Marine and Petroleum Geology 116 (2020) 104316

Contents lists available at ScienceDirect

Marine and Petroleum Geology

journal homepage: www.elsevier.com/locate/marpetgeo

Research paper

# Garnet trace element geochemistry as a sediment provenance indicator: An example from the Qaidam basin, northern Tibet

Dongming Hong[a], Xing Jian[a,*], Ling Fu[b], Wei Zhang[a]

[a] State Key Laboratory of Marine Environmental Science, College of Ocean and Earth Sciences, Xiamen University, Xiamen, 361102, PR China
[b] Research Institute of Petroleum Exploration and Development (RIPED), PetroChina, Beijing, 100083, PR China

ARTICLE INFO

*Keywords:*
Sedimentary provenance analysis
Single-grain analysis
Heavy mineral
Garnet
Trace element geochemistry

ABSTRACT

Major element geochemistry of detrital garnet is a widely-used approach for sedimentary provenance analysis, in particular for unravelling parent-rock lithology of siliciclastic sediments. However, garnets from felsic crystalline rocks (e.g., intermediate–acidic igneous rocks and metapelites) often have similar major element composition. This results in ambiguity of provenance interpretation in most cases. Here, we collect trace element data of garnets from different rock types to explore the feasibility of detrital garnet trace element geochemistry in sediment provenance analysis. The Qaidam basin in northern Tibet is taken as an example and provenance of Cenozoic sedimentary rocks therein is interpreted based on detrital garnet trace element composition. We find that garnets in intermediate–acidic igneous rocks have much higher heavy rare earth element (ΣHREE > 600 ppm) and yttrium (Y > 800 ppm) abundances than garnets in metapelites (ΣHREE < 300 ppm, Y < 500 ppm). Garnets in high-grade metapelites (e.g. granulite facies) usually have higher light rare earth element (ΣLREE > 4 ppm) and zinc (Zn > 150 ppm) abundances than garnets in low-, medium-grade metapelites (up to amphibolite facies). Based on these findings, we suggest that Fe- and Mn-rich detrital garnets in the Cenozoic sedimentary rocks from the northern Qaidam basin were probably derived from low-, medium-grade metapelites and Mg-rich, Ca-poor detrital garnets therein were most likely derived from granulite-facies metapelites. This provenance interpretation supports that the Qilian Mountains to the north was the major source for the northern Qaidam basin and major deformation style along the Altyn Tagh Fault to west have been dominated by large-amplitude lateral offset and extrusion, rather than crustal thickening and uplift during the early Cenozoic. This study emphasizes high potential of detrital garnet trace element geochemistry in provenance analysis and reconstruction of tectono-sedimentary evolution of clastic sedimentary basins.

## 1. Introduction

Sedimentary provenance analysis aims at reconstruction of parent-rock assemblages of sediment and physical and chemical conditions under which sediments formed (Johnsson, 1993; Basu, 2003; Li et al., 2004; Weltje and von Eynatten, 2004). Successful provenance analysis aspires to reconstruct all factors controlling the compositional and textural modifications that transformed a parent-rock to a final sedimentary deposit (Triebold et al., 2012). These factors mainly include source rock lithology, tectonic activity, relief and climate, as well as the modes of sediment transport, dispersal, and alteration on transit (e.g., Morton, 1993; Morton et al., 2005, 2011, Morton and Hallsworth, 1994, 1999; Meinhold et al., 2010; von Eynatten and Dunkl, 2012; Garzanti et al., 2015; Romans et al., 2016). Therefore, sedimentary provenance analysis is a valuable tool to reconstruct surface processes of the Earth over both modern and geological timescales; and its philosophy and concept has been widely applied in various aspects of geosciences, particularly in tectonics, paleoclimatology and petroleum geology (Dickinson, 1985, 1988; Hurst and Morton, 1988; Morton et al., 2001; Osae et al., 2006; Noble et al., 2012).

Sedimentary provenance analysis attempt to unravel the sediment form up processes and conditions based on the characteristics of the sediment itself. Traditional approaches rely on bulk sediment composition, including (1) modal composition analysis of sandstone framework grains (e.g., Blatt, 1967; Dickinson, 1970; Ingersoll et al., 1984); (2) heavy mineral analysis of sandstones (e.g., Pettijohn, 1963; Dill, 1995); and (3) whole rock major and trace element geochemistry analysis of sediments (e.g., McLennan et al., 1993). The growing database for different tectonic settings allowed for developing tectonic discrimination schemes based on bulk sediment petrographic and

* Corresponding author.
*E-mail address:* xjian@xmu.edu.cn (X. Jian).

https://doi.org/10.1016/j.marpetgeo.2020.104316
Received 15 October 2019; Received in revised form 14 February 2020; Accepted 26 February 2020
Available online 27 February 2020

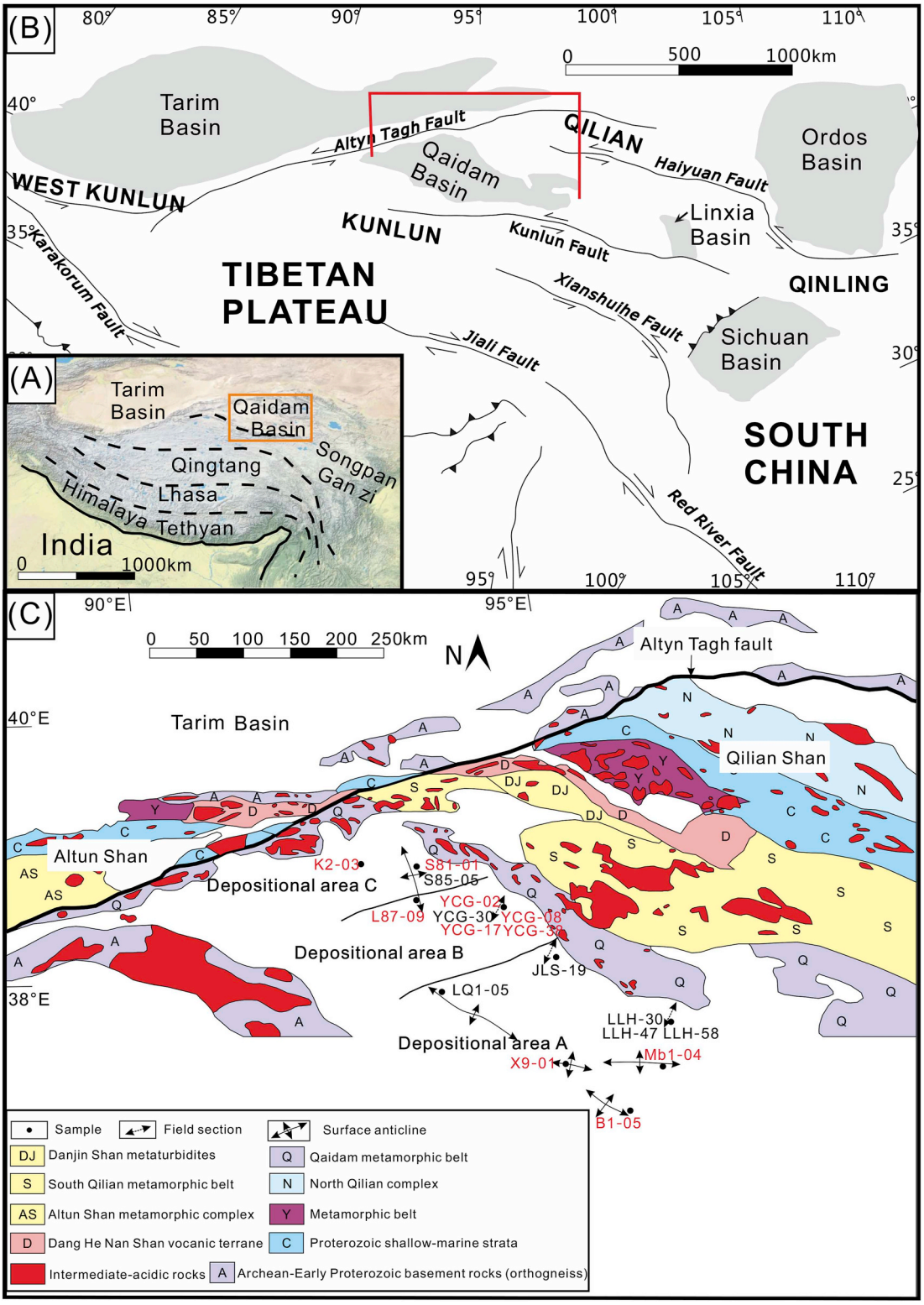


**Fig. 1.** (A, B) Geologic setting of the Qaidam basin; (C) sample locations (the geological background was modified from Gehrels et al. (2003) and the depositional areas A, B and C were proposed by Jian et al., 2013a.

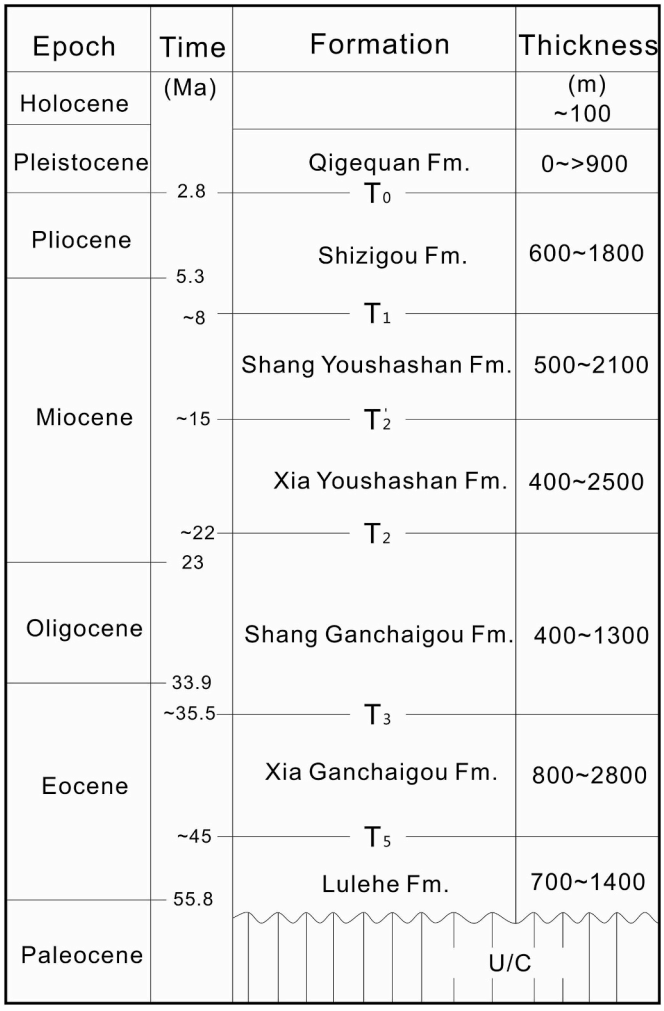


**Fig. 2.** The Cenozoic stratigraphic framework of the Qaidam basin (Ye et al., 1993; Sun et al., 2005; Wang et al., 2007). U/C: unconformity.

geochemical composition (e.g., Bhatia, 1983; Dickinson, 1985). However, results obtained by these traditional analysis methods generally reflect mixed signatures in the case of multiple sources. In addition, these methods might be unreliable for provenance analysis of highly modified sedimentary rocks (diagenetically or by weathering). Geochemistry (major, trace elements and isotopes) of individual sand-sized grains can in part overcome these issues. The potential of single-grain in-situ mineral-chemistry analysis to sedimentary provenance study was first summarized by Morton (1985) and further developed towards investigating the characteristics and variability of individual grains of a single mineral phase (e.g., feldspar, garnet, tourmaline, zircon, Cr-spinel, apatite and rutile) (Henry and Guidotti, 1985; Ross and Parrish, 1991; Clift et al., 2001; Basei et al., 2005; Chetel et al., 2005; Triebold et al., 2007; Meinhold et al., 2008; Lenaz et al., 2003, 2009; Coutand et al., 2010; Chew et al., 2011; von Eynatten and Dunkl, 2012; Bonova et al., 2018; Gillespie et al., 2018; Jian et al., 2013a, 2018; Jian et al., 2019a). The fast development and wide application of in-situ geochemical analysis techniques, such as electron microprobe analyses (EMPA) and laser-ablation inductively coupled plasma mass spectrometry (LA-ICP-MS), has made the single-grain method the most prominent in past decades (Fedo et al., 2003; Morton et al., 2004; Mange and Morton, 2007; Condie et al., 2009; Triebold et al., 2007; Meinhold, 2010).

Garnet is a common heavy mineral in sandy deposits. It is a relatively stable mineral under both weathering and burial diagenetic conditions (Morton and Hallsworth, 1999, 2007). Garnets from different protoliths or different temperature and pressure conditions display significantly different major and trace element composition (Bea and Montero, 1999; Krippner et al., 2014). Hence, detrital garnet is one of the most utilized heavy minerals for single-grain chemistry-based sedimentary provenance analysis (Morton et al., 2004; Čopjaková et al., 2005; Mange and Morton, 2007; Takeuchi et al., 2008; Jian et al., 2013a; Hietpas et al., 2014; Tolosana-Delgado et al., 2018; Lenaz et al., 2018).

The general formula of garnet is $X_3Y_2(SiO_4)_3$, where X is the divalent element (e.g., $Ca^{2+}$, $Mg^{2+}$, $Fe^{2+}$, $Mn^{2+}$), Y is trivalent element (e.g., $Al^{3+}$, $Fe^{3+}$, $Cr^{3+}$, $V^{3+}$). Morton (1985) first proposed detrital garnet chemistry as a sedimentary provenance indicator by using major elements; after that, garnet major element geochemistry has been widely employed in lots of case studies (Teraoka et al., 1997, 1998; Morton et al., 2004a,b; Mange and Morton, 2007; Aubrecht et al., 2009; Hietpas et al., 2014; Jian et al., 2013a; Krippner et al., 2014; Huber et al., 2018). Proposed methods for garnet geochemical discrimination mainly include five types of ternary diagrams on the basis of Fe, Mn, Mg and Ca abundances (Krippner et al., 2014 and references therein). Based on a large amount of garnet major element data and a hierarchical discrimination approach involving three steps with linear discriminant analysis at each step, Tolosana-Delgado et al. (2018) recently proposed a new multivariate discrimination method to distinguish 5 major parent-rock types (eclogite-, amphibolite- and granulite-facies metamorphic, as well as ultramafic and igneous rocks).

The main problem for those major element-based parent-rock interpretation models is that garnets of different origins may have similar major element composition, i.e., have overlap fields in those ternary diagrams. For example, the widely-used Mange and Morton (2007) method cannot be applied to accurately discriminate garnets derived from intermediate-acidic igneous rocks and granulite-facies metapelitic rocks, both of which show relatively Mg-rich, Ca-poor and Fe + Mn-rich (Type A, in the diagram of Mange and Morton (2007), the same below). And garnets of intermediate-acidic igneous rocks also usually cannot be distinguished from the ones of intermediate or low metapelite rocks (Type Bi and Type Bii, Krippner et al. (2014)). By contrast, little attention has been paid to the application of detrital garnet trace elements in sedimentary provenance analysis so far. Trace element data of 13 detrital garnet grains were first reported from the Lower Carboniferous Culm sediments, Bohemian Massif (Čopjaková et al., 2005), which are characterized by light rare earth elements (LREE) depletion, negative Eu anomalies and Y and heavy rare earth elements (HREE) enrichment. Those detrital garnets were inferred to be sourced from granulite-facies metapelitic rocks. Lenaz et al. (2018) targeted detrital garnets from flysch strata in the SE Alps and Outer Dinarides and found that trace element contents can be very different in almandine-rich garnets from different sources. These preliminary studies demonstrate a high potential of detrital garnet trace element geochemistry in sediment provenance analysis.

In this study, we collect published trace element geochemical data of garnet from different crystalline rocks and propose garnet trace element-based provenance interpretation models. We apply new approach to trace parent-rocks for Mg-rich, Ca-poor, Fe + Mn-rich (Type A), Mg-poor, Ca-poor, Fe + Mn-rich (Type Bi) and Mg-poor, variable Ca, Fe + Mn-rich (Type Bii) detrital garnets of the Cenozoic sandstones from the northern Qaidam basin, northern Tibet (Fig. 1) on which major element geochemical data were obtained in a previous study (Jian et al., 2013a). The objectives are to: 1) unravel parent-rock lithology of the grains of Fe + Mn-rich garnet from the Qaidam basin and 2) have a better understanding of the feasibility of garnet trace element geochemistry in sedimentary provenance analysis.

## 2. Geologic setting

The Qaidam basin is a large continental sedimentary basin located in the northern Tibetan Plateau (Fig. 1A). The basin covers an area of

**Table 1**
Descriptions of the analyzed sandstone samples from the northern Qaidam basin.

| Samples | location | geographic coordinate | formation | depositional setting[a] | lithology | Q(%) | F(%) | L(%) |
|---|---|---|---|---|---|---|---|---|
| YCG-38 | Pingtai Fold | 38°27′33″N, 93°55′2″E | Shang Youshashan Fm. | delta facies | lithic sandstone | 57 | 7 | 36 |
| YCG-17 | Pingtai Fold | 38°28′50″, 93°55′23″E | Shang Ganchaigou Fm. | delta facies | feldspathic lithic sandstone | 44 | 26 | 29 |
| YCG-02 | Pingtai Fold | 38°30′3″N, 93°55′46″E | Xia Ganchaigou Fm. | delta facies | lithic sandstone | 55 | 6 | 39 |
| YCG-08 | Pingtai Fold | 38°29′36″N, 93°55′36″E | Xia Ganchaigou Fm. | delta facies | feldspathic lithic sandstone | 65 | 17 | 18 |
| S81-01 | No. 4 Lenghu | 38°43′11″N, 93°19′43″E | Lulehe Fm. | alluvial fan facies | feldspathic lithic sandstone | 55 | 20 | 25 |
| L87-09 | No. 5 Lenghu | 38°36′51″N, 93°20′53″E | Shang Ganchaigou Fm. | delta facies | lithic sandstone | 46 | 14 | 40 |
| K2-03 | No. 3 Lenghu | 38°43′33″N, 93°03′14″E | Shang Ganchaigou Fm. | alluvial fan facies | lithic feldspar sandstone | 52 | 35 | 13 |
| Mb1-04 | Mahai | 37°55′58″N, 94°40′52″E | Xia Ganchaigou Fm. | fluvial facies | feldspathic lithic sandstone | 69 | 8 | 23 |
| X9-01 | Mahai | 37°56′18″N, 94°11′45″E | Shang Ganchaigou Fm. | delta facies | lithic sandstone | 50 | 10 | 40 |
| B1-05 | Beilingqiu | 37°46′2″N, 94°22′15″E | Shang Youshashan Fm. | fluvial/delta facies | lithic sandstone | 46 | 9 | 45 |

[a] The depositional settings and Q-F-L volume percentage data are modified from Jian et al., 2013a. Q: quartz; F: feldspar; L: lithic fragment.

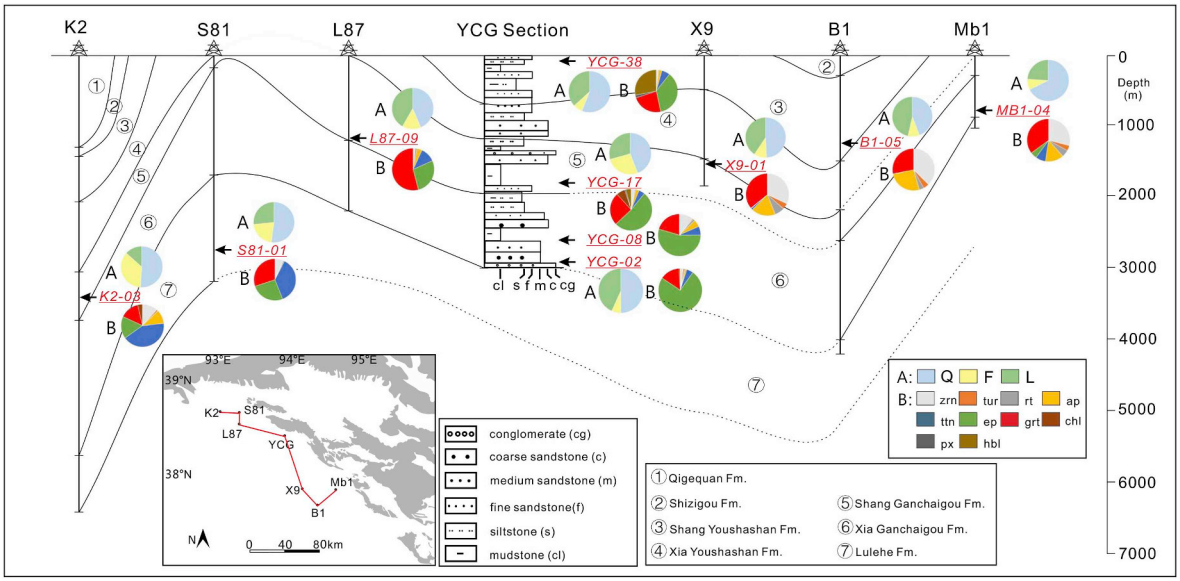


**Fig. 3.** Stratigraphic correlation of the investigated outcrop section and drilling wells and previously reported petrography and heavy mineral results (Jian et al., 2013a) for the analyzed sandstone samples. For sample locations, see Fig. 1C. Q: quartz, F: feldspar, L: lithic fragments; zrn: zircon, tur: tourmaline, rt: rutile, ap: apatite, ttn: titanite, ep: epidote, grt: garnet, chl: chlorite, px: pyroxene, hbl: hornblende.

about 120,000 km$^2$, sits 2.7–3.0 km above sea level and has preserved 3–16 km thick Mesozoic and Cenozoic sedimentary strata (Jian, 2013; Jian et al., 2014, 2019; Zhang et al., 2018). The basin is surrounded by mountains on three sides (Fig. 1B), i.e., the East Kunlun Mountains to the south, the Qilian Mountains to the east and the Altun Mountains to the northwest. Formation of the Qaidam basin is considered to be a result of the convergent system at the northern margin of the Tibetan Plateau (Tapponnier et al., 2001), which is generally associated with the India-Asia collision and subsequent rise, thickening, shortening, lateral extrusion of the Tibetan Plateau (Harrison et al., 1992; Tapponnier et al., 2001; Yin et al., 2002; Yue et al., 2003; Zhuang et al., 2011; Jian et al., 2018). Consequently, it developed a series of thrust fold belts in the northwest-southeast direction in the basin and reverse faults along the Eastern Kunlun and Qilian Mountains.

The South Qilian terranes and the southern flanks of the Altun Mountains (Fig. 1C) were proposed to be the source regions for the Cenozoic sediments in the northern Qaidam basin (Zhuang et al., 2011; Jian et al., 2013a, Jian et al., 2013b; Jian et al., 2018; Lu et al., 2018). The South Qilian terrane is mainly composed of Upper Proterozoic to Lower Paleozoic metamorphic rocks (mainly metapelites and subordinate acidic metavolcanics). The basement of the South Qilian terrane, mainly exposed as the Proterozoic Dakendaban Group, is characterized by variable-grade metamorphic rocks (low- to high-grade metamorphic rocks) (Fig. 1C). The North Qaidam orogenic belt is represented by a Paleozoic metamorphic belt, consisting of pelitic shallow sea (meta-)sediments, mylonite and granite, and a small number of eclogite and garnet peridotite bodies (Gehrels et al., 2003; Song et al., 2003a, b, 2005; Mattinson et al., 2006; Song et al., 2006; Yang et al., 2006; Mattinson et al., 2007; Song et al., 2007a, b; Zhang et al., 2008; Mattinson et al., 2009; Menold et al., 2009). The northern flanks of the Altun Mountains host of granite, some metamorphic complex rocks, Ordovician metasedimentary rocks and Jurassic sedimentary rocks, while the southern flanks are dominated by Paleozoic and Mesozoic granite rocks (Zhang and Gou, 1993; Gehrels et al., 2003).

The Cenozoic strata of the Qaidam basin can be divided into 7 stratigraphic units (Fig. 2) according to the basin-wide lithostratigraphic framework, the microfossil studies, magnetostratigraphy and isotope geochronology (Ye et al., 1993; Sun et al., 2005; Wang et al., 2007), as follows: (1) Lulehe Formation (Paleocene to early Eocene, ?–~45 Ma); (2) Xia Ganchaigou Formation (middle to late Eocene, ~45–~35.5 Ma); (3) Shang Ganchaigou Formation (late Eocene to Oligocene, ~35.5–~22 Ma); (4) Xia Youshashan Formation (early to middle Miocene, ~22–~15 Ma); (5) Shang Youshashan Formation (middle to late Miocene, ~15–~8 Ma); (6) Shizigou Formation (late Miocene to Pliocene, ~8–2.8 Ma); and (7) Qigequan Formation (Quaternary, 2.8 Ma–present).

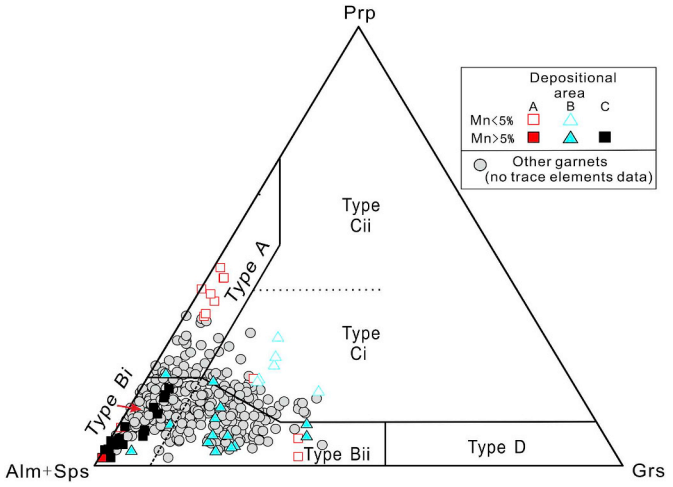


**Fig. 4.** Major element composition plots for the analyzed 10 sandstone samples in the Alm + Sps-Grs-Prp discrimination diagram after Mange and Morton (2007). A—granulite-facies metasediments and intermediate felsic igneous rocks or charnockites (mainly derived from crust in depth, Mg-rich, Ca-poor), Bi—intermediate to felsic igneous rocks (Fe-rich, Mn-rich), Bii—medium-low metasedimentary rocks, amphibolite-facies (Mg-poor, variable Ca), Ci—metabasic rocks, Type Cii—ultramafic rocks (Mg-rich, boundary between Ci and Cii is 50% magnesium content), D—low-grade metabasic rocks or contact metasomatic metamorphic rock (Ca-rich). All the garnet major elements data are shown in Table A1. Alm, Sps, Grs and Prp are almandine, spessartite, grossularite and pyrope, respectively, show the end-member elements percentage of garnet.

## 3. Samples and analytical methods

### 3.1. Sample description

All the analyzed garnet grains were separated from 10 sandstone samples (Fig. 1C), including 5 lithic sandstones, 4 feldspathic lithic sandstones and one lithic feldspar sandstone (Table 1). These sandstone samples were previously analyzed for framework petrography, heavy mineral assemblages and major element composition of detrital garnet (Jian et al., 2013a). The related results are shown in Fig. 3 and Figs. B1–B3 (in Appendix B). Most detrital grains of the Cenozoic sandstones are angular to subangular and poorly to moderately sorted. The framework detritus is dominated by quartz and lithic fragments, with abundances (in Q-F-L diagram) ranging from 36% to 74% and from 8% to 51%, respectively. The lithic fragments are dominated by metasedimentary lithic fragments (Jian et al., 2013a). The heavy mineral mainly includes garnet, epidote, zircon, tourmaline and apatite, indicating a major derivation of metamorphic rocks (Jian et al., 2013a).

The detrital garnets are characterized by high almandine and spessartine end-member contents (Fig. 4; Jian et al., 2013a). The analyzed detrital garnet grains in this study include Fe + Mn-rich, Mg-rich and Ca-poor (Type A) garnets from samples L87-09, X9-01, Mb1-04, B1-05, Fe + Mn-rich, Mg-poor and Ca-poor (Type Bi) garnets from samples S81-01, K2-03, YCG-02, B1-05, Mb1-04, Fe + Mn-rich, Mg-poor and variable Ca (Type Bii) garnets from samples X9-01, YCG-02, YCG-08, YCG-17, YCG-38, Fe + Mn-poor, Mg-rich and Ca-rich (Type Ci) garnets from samples YCG-02, YCG-08, YCG-17, Mb1-04 (Table A1 in Appendix A). Major element composition data and corresponding parent-rock interpretations of these detrital garnets are shown in Table 2.

### 3.2. Analytical methods

Typical Type A, B and Ci detrital garnet grains (Fig. 4) were selected for trace element analysis. Note that most analyzed grains are plotted far from the boundaries of the different fields in the Mange and Morton (2007) diagram (Fig. 4). The geochemical data of garnets were measured at the Ministry of Education Key Laboratory of Orogenic Belts and Crustal Evolution, Peking University. Major element analyses had been already carried out on JEOL JXA-8100 EPMA (Jian et al., 2013a) with 15 kv acceleration voltage, 1 μm beam spot and 1 A beam current conditions. Trace element analysis was undertaken on an Agilent 7500a ICP-MS, laser (with a 193 nm ArF-excimer laser) and GeoLas200M laser-ablation system. The laser beam spot was about 44 μm, the depth of laser ablation was 32 μm, the energy density was 15 J/cm$^2$ and the laser repetition rate was 4 Hz, used He as carrier gas. All the trace element analysis spots are consistent with those for the major element analysis. The synthetic silicate glass NIST SRM 610 was used as the reference material (Song et al., 2007a), and $^{29}$Si was used as the internal standard. The grain sizes and ablation locations of the analyzed garnets are listed in Table 3.

### 3.3. Cluster analysis

Cluster analysis is a useful statistic method for classifying data into different classes or clusters. Objects in the same cluster have similarities, while objects in different clusters have great differences (Vermunt and Magidson, 2002). Here, the SPSS (Statistical Product and Service Solutions) program was used to conduct cluster analysis and k-means clustering algorithm was employed to classify the 51 detrital garnet grains in this study.

## 4. Results

Detrital garnets fallen within the fields of Type A, Bi and Bii (Fig. 4) have similar patterns of rare earth elements (REE) (Fig. 5A and B), i.e., depletion in LREE, enrichment in HREE and negative Eu anomalies (Eu/Eu* = $Eu_N/0.5(Sm_N + Gd_N)$, with the subscript N denoting chondrite-normalized values from McDonough and Sun (1995)). However, these detrital garnet grains have different REE abundances. Twenty-two Type Bi garnet grains have ΣHREE of 3–1505 ppm, ΣLREE of 0.4–39 ppm, Eu/Eu* ratio of 0.01–0.86, Zn contents of 3–378 ppm, Y contents of 6–2786 ppm; twelve Type Bii garnet grains have ΣHREE of 7–1018 ppm, ΣLREE of 0.1–4 ppm, Eu/Eu* ratio of 0.2–1.4, Zn contents of 14–61 ppm, Y contents of 17–2245 ppm; nine Type A garnet grains have ΣHREE of 32–142 ppm, ΣLREE of 1–16 ppm, Eu/Eu* ratio of 0.04–0.24, Zn contents of 38–285 ppm, Y contents of 45–262 ppm. In addition, some Type A garnets show a different REE pattern, i.e., middle REE are more abundant than heavy REE, with $Gd_N/Yb_N$ ratios >1. For the garnet grains that have been interpreted to be derived from intermediate-acidic igneous rocks (Type A or Type Bi) based on major element analysis, only grains YCG-02.9, YCG-02.32, S81–01.1, S81–01.12, S81–01.25, K2-03.2, K2-03.13, K2-03.21, K2-03.22 have ΣHREE over 500 ppm and Y content greater than 800 ppm. The Type Bii garnet grains, which have been interpreted to be derived from low-, medium-grade metapelites, have ΣHREE below 500 ppm and Y < 800 ppm.

Patterns of the eight Type Ci garnet grains show the following features: depletion in LREE, enrichment in HREE and no Eu anomalies or slight Eu negative anomalies (Fig. 5C). These garnet grains have ΣHREE of 1–64 ppm, ΣLREE of 0.2–8 ppm, Eu anomaly values of 0.3–2, Zn contents of 15–135 ppm, and Y contents of 24–114 ppm.

According to the new major elements-based garnet discrimination scheme of Tolosana-Delgado et al. (2018), twenty-seven detrital garnet grains therein were interpreted to be derived from amphibolite-facies

**Table 2**
Major element data and the discriminant results based on the ternary diagram of Mange and Morton (2007) and the discrimination scheme of Tolosana-Delgado et al. (2018) for the analyzed detrital garnet grains in this study.

| Garnets | original data (in wt%) | | | | | | | | | | | | Mange and Morton (2007) | integrated probabilities (Tolosana-Delgado et al., 2018) |
|---|---|---|---|---|---|---|---|---|---|---|---|---|---|---|
| | $K_2O$ | $Na_2O$ | MgO | $Cr_2O_3$ | CaO | $SiO_2$ | $Al_2O_3$ | MnO | $TiO_2$ | FeO | NiO | Total | | |
| YCG-38.17 | 0 | 0.04 | 0.75 | 0 | 6.94 | 37.13 | 20.88 | 12.71 | 0 | 21.3 | 0 | 99.76 | low-, medium-grade metapelites | amphibolite-facies metamorphic rocks |
| YCG-38.19 | 0 | 0 | 1.06 | 0 | 8.05 | 37.63 | 21.57 | 9.47 | 0.09 | 22.7 | 0.02 | 100.59 | low-, medium-grade metapelites | amphibolite-facies metamorphic rocks |
| YCG-38.36 | 0 | 0.04 | 3.29 | 0 | 5.97 | 37.58 | 21.2 | 3.88 | 0.02 | 27.73 | 0 | 99.71 | low-, medium-grade metapelites | amphibolite-facies metamorphic rocks |
| YCG-17.14 | 0.01 | 0.06 | 4.7 | 0 | 8.3 | 37.9 | 20.89 | 0.41 | 0.25 | 26.72 | 0.01 | 99.24 | metabasic rocks | granulite-facies metamorphic rocks |
| YCG-17.16 | 0.01 | 0.07 | 1.25 | 0 | 6.23 | 36.79 | 20.82 | 10.45 | 0.15 | 23.74 | 0.04 | 99.56 | low-, medium-grade metapelites | amphibolite-facies metamorphic rocks |
| YCG-17.23 | 0 | 0 | 0.99 | 0 | 8.02 | 37.23 | 21.39 | 5.97 | 0.02 | 26.27 | 0 | 99.89 | low-, medium-grade metapelites | amphibolite-facies metamorphic rocks |
| YCG-17.30 | 0 | 0.06 | 1.68 | 0 | 6.42 | 37.25 | 21.18 | 3.37 | 0.01 | 29.54 | 0 | 99.51 | low-, medium-grade metapelites | amphibolite-facies metamorphic rocks |
| YCG-02.9 | 0 | 0 | 1.64 | 0 | 7.38 | 37.38 | 21.07 | 6.34 | 0.04 | 25.91 | 0.03 | 99.8 | low-, medium-grade metapelites | amphibolite-facies metamorphic rocks |
| YCG-02.17 | 0 | 0.07 | 4.62 | 0 | 5.36 | 37.41 | 20.88 | 3.85 | 0.08 | 27.19 | 0 | 99.46 | metabasic rocks | amphibolite-facies metamorphic rocks |
| YCG-02.25 | 0.01 | 0 | 6.22 | 0 | 8.27 | 38.15 | 21.68 | 0.64 | 0.08 | 23.98 | 0 | 99.03 | metabasic rocks | granulite-facies metamorphic rocks |
| YCG-02.32 | 0 | 0.08 | 0.73 | 0 | 1.69 | 36.61 | 21.07 | 11.69 | 0.06 | 27.5 | 0 | 99.43 | intermediate-acidic igneous rocks | amphibolite-facies metamorphic rocks |
| YCG-02.34 | 0 | 0 | 2.64 | 0.02 | 6.02 | 37.1 | 20.49 | 6.62 | 0.07 | 26.23 | 0.08 | 99.26 | low-, medium-grade metapelites | amphibolite-facies metamorphic rocks |
| YCG-02.39 | 0.03 | 0.02 | 2.19 | 0.03 | 3.2 | 36.85 | 20.69 | 11.65 | 0.14 | 24.75 | 0.03 | 99.59 | intermediate-acidic igneous rocks | amphibolite-facies metamorphic rocks |
| YCG-08.3 | 0 | 0.01 | 4.28 | 0.01 | 12.51 | 38.52 | 21.84 | 2.2 | 0.04 | 20.98 | 0.03 | 100.41 | metabasic rocks | amphibolite-facies metamorphic rocks |
| YCG-08.5 | 0.01 | 0.03 | 4.97 | 0.02 | 7.56 | 37.92 | 21.47 | 1.07 | 0.32 | 25.84 | 0.05 | 99.25 | metabasic rocks | granulite-facies metamorphic rocks |
| YCG-08.24 | 0 | 0 | 1.65 | 0 | 12.84 | 37.99 | 21.59 | 4.22 | 0.02 | 21.83 | 0.04 | 100.18 | low-, medium-grade metapelites | amphibolite-facies metamorphic rocks |
| YCG-08.30 | 0 | 0 | 2.3 | 0.03 | 12.97 | 37.51 | 21.04 | 2.64 | 0 | 22.75 | 0 | 99.24 | low-, medium-grade metapelites | amphibolite-facies metamorphic rocks |
| YCG-08.32 | 0 | 0.03 | 5.83 | 0 | 8.37 | 38.59 | 21.83 | 1.18 | 0.05 | 24.27 | 0 | 100.15 | metabasic rocks | granulite-facies metamorphic rocks |
| YCG-08.34 | 0.02 | 0.05 | 7.39 | 0.02 | 7.73 | 38.7 | 22.06 | 0.62 | 0.07 | 22.97 | 0 | 99.62 | metabasic rocks | granulite-facies metamorphic rocks |
| S81–01.1 | 0 | 0.03 | 1.56 | 0 | 1.9 | 36.9 | 20.57 | 13.05 | 0 | 26.16 | 0.01 | 100.18 | intermediate-acidic igneous rocks | amphibolite-facies metamorphic rocks |
| S81–01.4 | 0.01 | 0.01 | 3.93 | 0 | 1.78 | 37.42 | 20.93 | 6.86 | 0.02 | 28.62 | 0 | 99.59 | intermediate-acidic igneous rocks | amphibolite-facies metamorphic rocks |
| S81–01.12 | 0 | 0 | 3.21 | 0.04 | 1.58 | 37.14 | 20.45 | 10.61 | 0.04 | 26.87 | 0 | 99.94 | intermediate-acidic igneous rocks | amphibolite-facies metamorphic rocks |
| S81–01.14 | 0 | 0.06 | 1.28 | 0 | 0.09 | 36.84 | 21.67 | 14.43 | 0.03 | 26.14 | 0.01 | 100.56 | intermediate-acidic igneous rocks | igneous rocks |
| S81–01.15 | 0 | 0.01 | 2.06 | 0.03 | 0.47 | 36.55 | 20.78 | 12.84 | 0 | 27.01 | 0 | 99.75 | intermediate-acidic igneous rocks | igneous rocks |
| S81–01.21 | 0 | 0.01 | 4.38 | 0.03 | 1.9 | 37.16 | 20.89 | 3.59 | 0.11 | 31.41 | 0.04 | 99.51 | intermediate-acidic igneous rocks | amphibolite-facies metamorphic rocks |
| S81–01.25 | 0 | 0.02 | 3.81 | 0 | 1.86 | 37.08 | 20.74 | 5.08 | 0.03 | 30.69 | 0.04 | 99.35 | intermediate-acidic igneous rocks | amphibolite-facies metamorphic rocks |
| S81–01.26 | 0.02 | 0.04 | 1.22 | 0.01 | 0.33 | 36.06 | 20.35 | 14.55 | 0 | 26.41 | 0 | 99 | intermediate-acidic igneous rocks | igneous rocks |
| S81–01.28 | 0 | 0.02 | 0.81 | 0.03 | 0.09 | 36.61 | 20.64 | 14.93 | 0 | 26.89 | 0 | 100.01 | intermediate-acidic igneous rocks | igneous rocks |
| L87–09.21 | 0 | 0.03 | 5.18 | 0 | 1.33 | 37.46 | 21.11 | 4.13 | 0.05 | 30.71 | 0 | 100 | high-grade granulite-facies metapelites or intermediate-acidic igneous rocks | amphibolite-facies metamorphic rocks |
| K2-03.1 | 0.03 | 0.01 | 1.84 | 0.03 | 1.84 | 37.04 | 20.96 | 10.69 | 0.01 | 27.64 | 0 | 100.09 | intermediate-acidic igneous rocks | amphibolite-facies metamorphic rocks |
| K2-03.2 | 0 | 0.03 | 1.86 | 0.01 | 1.74 | 37.37 | 21.51 | 12.75 | 0.04 | 25.34 | 0.02 | 100.67 | intermediate-acidic igneous rocks | amphibolite-facies metamorphic rocks |
| K2-03.5 | 0.01 | 0.01 | 0.86 | 0 | 0.22 | 36.85 | 21.03 | 16.36 | 0 | 25.49 | 0.03 | 100.87 | intermediate-acidic igneous rocks | igneous rocks |
| K2-03.9 | 0 | 0.03 | 1.45 | 0.02 | 0.54 | 36.91 | 20.97 | 10.71 | 0.1 | 29.72 | 0.02 | 100.46 | intermediate-acidic igneous rocks | igneous rocks |
| K2-03.13 | 0 | 0.04 | 1.09 | 0.03 | 0.5 | 36.96 | 21.51 | 11.02 | 0.02 | 30 | 0.04 | 101.21 | intermediate-acidic igneous rocks | igneous rocks |
| K2-03.14 | 0 | 0 | 2.74 | 0.09 | 2.03 | 37.8 | 21.68 | 10.45 | 0.02 | 25.77 | 0 | 100.58 | intermediate-acidic igneous rocks | amphibolite-facies metamorphic rocks |
| K2-03.21 | 0 | 0 | 1.1 | 0 | 0.96 | 36.78 | 21.22 | 11.07 | 0.01 | 29.09 | 0.02 | 100.24 | intermediate-acidic igneous rocks | amphibolite-facies metamorphic rocks |
| K2-03.22 | 0.01 | 0 | 0.41 | 0 | 0.66 | 36.63 | 20.88 | 15.3 | 0.06 | 25.65 | 0 | 99.6 | intermediate-acidic igneous rocks | igneous rocks |
| Mb1-04.10 | 0.01 | 0 | 9.05 | 0.02 | 1.41 | 38.13 | 21.03 | 0.71 | 0.02 | 28.94 | 0.08 | 99.4 | high-grade granulite-facies metapelites or intermediate-acidic igneous rocks | granulite-facies metamorphic rocks |
| Mb1-04.13 | 0.03 | 0 | 2.11 | 0 | 0.48 | 36.52 | 20.67 | 0.08 | 0 | 39.35 | 0.02 | 99.26 | intermediate-acidic igneous rocks | amphibolite-facies metamorphic rocks |
| Mb1-04.15 | 0.04 | 0.01 | 9.66 | 0.06 | 2.42 | 38.6 | 21.63 | 0.54 | 0.01 | 26.62 | 0 | 99.59 | high-grade granulite-facies metapelites or intermediate-acidic igneous rocks | granulite-facies metamorphic rocks |
| Mb1-04.31 | 0 | 0 | 9.14 | 0.02 | 1.39 | 38.2 | 21.24 | 0.47 | 0.05 | 28.59 | 0.03 | 99.14 | high-grade granulite-facies metapelites or intermediate-acidic igneous rocks | granulite-facies metamorphic rocks |
| Mb1-04.38 | 0 | 0.02 | 4.81 | 0.04 | 8.22 | 37.66 | 21.11 | 0.52 | 0.02 | 26.68 | 0 | 99.08 | metabasic rocks | granulite-facies metamorphic rocks |
| X9-01.12 | 0 | 0.03 | 0.52 | 0.06 | 13 | 37.86 | 21.73 | 1.15 | 0.1 | 25.78 | 0 | 100.23 | low-, medium-grade metapelites | amphibolite-facies metamorphic rocks |
| X9-01.19 | 0.02 | 0.04 | 9.42 | 0.11 | 2.6 | 38.91 | 21.56 | 0.77 | 0.04 | 26.55 | 0 | 100.02 | high-grade granulite-facies metapelites or intermediate-acidic igneous rocks | granulite-facies metamorphic rocks |
| X9-01.24 | 0.02 | 0 | 9.84 | 0.07 | 1.89 | 38.44 | 21.25 | 0.5 | 0.01 | 27.14 | 0 | 99.16 | high-grade granulite-facies metapelites or intermediate-acidic igneous rocks | granulite-facies metamorphic rocks |

(*continued on next page*)

**Table 2** (*continued*)

| Garnets | original data (in wt%) | | | | | | | | | | | Mange and Morton (2007) | integrated probabilities (Tolosana-Delgado et al., 2018) |
|---|---|---|---|---|---|---|---|---|---|---|---|---|---|
| | $K_2O$ | $Na_2O$ | MgO | $Cr_2O_3$ | CaO | $SiO_2$ | $Al_2O_3$ | MnO | $TiO_2$ | FeO | NiO | Total | | |
| X9-01.27 | 0.01 | 0 | 1.51 | 0.01 | 12.98 | 37.3 | 20.64 | 1.68 | 0.08 | 24.81 | 0 | 99.01 | low-, medium-grade metapelites | amphibolite-facies metamorphic rocks |
| X9-01.29 | 0 | 0.02 | 11.28 | 0.07 | 1.91 | 38.9 | 21.68 | 0.39 | 0.03 | 24.82 | 0 | 99.09 | high-grade granulite-facies metapelites or intermediate-acidic igneous rocks | granulite-facies metamorphic rocks |
| X9-01.34 | 0.03 | 0 | 11.68 | 0.11 | 1.31 | 38.82 | 21.06 | 0.35 | 0 | 26.05 | 0.03 | 99.44 | high-grade granulite-facies metapelites or intermediate-acidic igneous rocks | granulite-facies metamorphic rocks |
| B1-05.16 | 0.01 | 0 | 11.25 | 0.01 | 1.24 | 39.38 | 22.36 | 0.41 | 0 | 25.18 | 0.02 | 99.86 | high-grade granulite-facies metapelites or intermediate-acidic igneous rocks | granulite-facies metamorphic rocks |
| B1-05.35 | 0 | 0 | 0.41 | 0 | 0.16 | 36.31 | 21.22 | 10.67 | 0.01 | 30.17 | 0.04 | 98.99 | intermediate-acidic igneous rocks | igneous rocks |
| B1-05.37 | 0.02 | 0.03 | 1.17 | 0.05 | 0.36 | 36.28 | 20.2 | 17.29 | 0.08 | 23.12 | 0 | 98.6 | intermediate-acidic igneous rocks | igneous rocks |

metamorphic rocks, fourteen grains were interpreted to be derived from granulite-facies metamorphic rocks and ten grains were interpreted to be derived from igneous rocks. The new interpretation indicates that most of these detrital garnets were probably sourced from metamorphic rather than igneous rocks, compared with the results depending on the ternary diagram of Mange and Morton (2007) (Table 2).

## 5. Discussion

### 5.1. Trace element geochemistry of garnets in felsic crystalline rocks

Published trace element data of 430 garnets from different rock types (granite, granulite-facies metapelite, and amphibolite-facies metapelite) were collected for comparison (Fig. 6, Table A2). Garnets in the granulite-facies metapelites show two types of REE patterns: (1) LREE depletion, HREE enrichment (or HREE depletion relative to MREE) and negative Eu anomaly, and (2) LREE and HREE depletion, MREE enrichment and no Eu anomaly (Bea et al., 1997, 1999; Hermann and Rubatto, 2003; Buick et al., 2010; Taylor and Stevens, 2010; Orejana et al., 2011; Clarke et al., 2013; Jiao et al., 2013). The garnets of granulite-facies metapelites in the Kinzigite Formation of the Ivrea-Verbano zone, northwest Italy also show the former typical features (Bea and Montero, 1999). There are also two types of REE distribution patterns for garnets in amphibolite-facies metapelites, i.e., (1) LREE depletion, HREE enrichment and negative Eu anomaly, which is similar to the REE distribution pattern of garnet from granite; and (2) LREE depletion, HREE enrichment and no Eu anomaly (Bea et al., 1997, 1999; Buick et al., 2010; Orozbaev et al., 2015; Gulbin, 2016). In addition, garnets derived from both granites and metapelites show the REE pattern of LREE depletion, HREE enrichment and negative Eu anomaly (Fig. 6A) (Bray 1988; Jung and Hellebrand, 2006; Villaros et al., 2009; Gao et al., 2012; Xu et al., 2013; Yang et al., 2013; Hönig et al., 2014).

It is worth noting that garnets from granites and metapelites have different REE abundances. Granite-derived garnet has higher ΣHREE (range: 201–9951 ppm), most more than 600 ppm, especially for thoes garnets from A-type granites than metapelite-derived garnet (ΣHREE range: 15–1661 ppm, most less than 600 ppm) (Table 4). This can be explained as follows. LREE are relatively incompatible elements and tend to enter melt rather than crystals (Villaros et al., 2009; Yang et al., 2013; Hönig et al., 2014). Magmatic garnets crystallize directly from the melt and have good euhedral crystal shapes and hence granite garnets will be significantly rich in HREE and Y (Gao et al., 2012; Hönig et al., 2014; Gulbin, 2016).

Here we propose that detrital garnets with ΣHREE greater than 600 ppm are probably derived from granitic rocks, while detrital garnets with ΣHREE less than 600 ppm are probably from metapelites (granulite-facies and amphibolite-facies). In addition, granulite-facies metapelite rock-derived garnets can be further distinguished from amphibolite-facies metapelite-derived garnets based on the ΣLREE contents (Fig. 6B). Note that this proposition is for those detrital garnets with Fe + Mn-rich, Mg-rich and Ca-poor abundances (i.e. of felsic crystalline rock origin). Previous studies realized that the growth zonation of a single garnet grain displays different trace element composition (Faryad et al., 2018). For example, garnets from A-type granites, highly fractionated granitic pegmatites and some biotite granodiorites generally indicate outward decrease of Y and REE (Smeds, 1994; Whitworth and Feely, 1994; Dorais and Tubrett, 2012; Müller et al., 2012; Hönig et al., 2014). In contrast, garnets from peraluminous S-type granites shows increasing Y and REE contents from the core toward the rim (Sevigny, 1993; Bea, 1996). However, most geochemical data of core and rim parts in a single garnet grain tend to be plotted in the same fields in our proposed discrimination diagram, for both metapelite- and granite-derived garnets (Fig. 7). Furthermore, our previous studies on different parts of single detrital garnet grains from the Qaidam basin indicate that most detrital garnet grains have

**Table 3**
Representative trace element data of the analyzed detrital garnets (unit: ppm).

| Garnets | Grain Size[a] (μm) | Ablation Location | Zn | Y | La | Ce | Pr | Nd | Sm | Eu |
|---|---|---|---|---|---|---|---|---|---|---|
| **YCG-38.17** | 261.9 | Rim | 45.7 | 2244.92 | <0.029 | <0.027 | <0.028 | 0.244 | 2.72 | 1.273 |
| **YCG-38.19** | 401.5 | Rim | 24.48 | 346.16 | <0.040 | <0.043 | <0.0171 | <0.127 | 0.169 | 0.217 |
| **YCG-38.36** | 296.4 | Rim | 45.99 | 341.46 | <0.0244 | <0.028 | <0.0224 | <0.111 | <0.207 | 0.122 |
| YCG-17.14 | 147.9 | Rim | 90.72 | 23.68 | <0.0161 | <0.026 | <0.0295 | 0.16 | <0.173 | 0.572 |
| **YCG-17.16** | 229.0 | Core | 21.55 | 349.35 | 0.036 | 0.043 | <0.025 | <0.126 | 0.248 | 0.488 |
| **YCG-17.23** | 220.5 | Core | 27.22 | 188.76 | <0.030 | <0.0230 | <0.0181 | <0.174 | 0.19 | 0.162 |
| **YCG-17.30** | 184.0 | Core | 24.91 | 647.53 | <0.0180 | 0.038 | <0.030 | <0.245 | <0.255 | 0.154 |
| **YCG-02.9** | 157.2 | Core | 27.67 | 723.9 | 0.207 | 0.348 | 0.047 | 0.217 | 0.261 | 0.217 |
| YCG-02.17 | 147.5 | Core | 14.81 | 39.6 | <0.0231 | <0.0154 | <0.0244 | 0.11 | <0.174 | 0.056 |
| YCG-02.25 | 142.8 | Core | 123.02 | 101.82 | <0.047 | <0.0271 | <0.0175 | <0.183 | 1.66 | 1.636 |
| YCG-02.32 | 158.1 | Rim | 170.54 | 2785.97 | <0.030 | 0.0262 | <0.0171 | 0.189 | 3.79 | 0.096 |
| **YCG-02.34** | 190.0 | Core | 45.55 | 16.61 | <0.036 | 0.041 | <0.0241 | 0.152 | 0.614 | 0.375 |
| **YCG-02.39** | 123.3 | Rim | 17.08 | 181.3 | <0.035 | 0.066 | 0.078 | 1.67 | 5.37 | 3.44 |
| YCG-08.3 | 119.3 | Rim | 83.73 | 114 | <0.030 | <0.035 | <0.0253 | 0.154 | 0.155 | 0.113 |
| YCG-08.5 | 156.0 | Core | 94.78 | 50.18 | 0.023 | 0.122 | 0.076 | 1.99 | 1.96 | 1.87 |
| **YCG-08.24** | 111.4 | Core | 26.57 | 176.74 | 0.097 | 0.158 | 0.0472 | <0.167 | 0.56 | 0.411 |
| **YCG-08.30** | 113.8 | Core | 61.09 | 59.35 | <0.039 | 0.033 | <0.023 | <0.124 | <0.146 | 0.268 |
| YCG-08.32 | 172.6 | Core | 45.5 | 74.1 | <0.0207 | <0.034 | <0.0243 | 0.321 | 0.488 | 0.259 |
| YCG-08.34 | 123.7 | Rim | 134.74 | 108.33 | <0.028 | <0.026 | <0.0207 | <0.137 | 0.262 | 0.471 |
| S81–01.1 | 387.0 | Rim | 59.17 | 812.29 | <0.030 | <0.034 | <0.0201 | <0.149 | 0.482 | <0.060 |
| **S81-01.4** | 320.6 | Rim | 36.76 | 250.9 | 0.0227 | 0.0375 | <0.0215 | 0.225 | 1.62 | 0.151 |
| S81–01.12 | 194.5 | Core | 39.11 | 485.71 | <0.036 | 0.145 | <0.0134 | 0.149 | 0.546 | 0.234 |
| **S81-01.14** | 196.2 | Rim | 249.34 | 575.02 | <0.0284 | <0.0269 | 0.0207 | <0.165 | 2.77 | <0.064 |
| S81–01.15 | 295.9 | Rim | 146.81 | 10.3 | <0.0222 | 0.056 | 0.0279 | <0.173 | 2.88 | 0.055 |
| **S81-01.21** | 389.7 | Rim | 35.7 | 54.12 | <0.0242 | 0.059 | 0.043 | 1.54 | 5.23 | 0.702 |
| S81–01.25 | 348.4 | Core | 35.52 | 1482.19 | <0.031 | <0.046 | 0.0212 | 0.173 | 0.91 | 0.45 |
| **S81-01.26** | 410.1 | Rim | 378.05 | 615.5 | 0.029 | 0.115 | 0.278 | 5.51 | 33.29 | <0.064 |
| S81–01.28 | 370.6 | Core | 127.33 | 5.66 | <0.0176 | <0.0235 | 0.0158 | 0.217 | 0.561 | <0.045 |
| L87–09.21 | 158.8 | Core | 38.3 | 261.86 | <0.028 | <0.026 | 0.0633 | 0.741 | 3.09 | 0.165 |
| **K2-03.1** | 160.5 | Core | 50 | 331.5 | <0.0241 | <0.0263 | <0.0294 | <0.154 | 0.367 | <0.054 |
| K2-03.2 | 170.9 | Rim | 59.51 | 1166.14 | 0.0165 | 0.028 | <0.0213 | <0.111 | 1.22 | <0.051 |
| K2-03.5 | 171.7 | Core | 95.44 | 130.43 | <0.0228 | 0.0232 | <0.0209 | 0.26 | 3.4 | <0.053 |
| **K2-03.9** | 152.8 | Core | 117.67 | 1056.82 | 0.0158 | <0.030 | <0.0263 | 0.28 | 3.86 | <0.033 |
| **K2-03.13** | 221.6 | Core | 96.78 | 813.96 | <0.033 | <0.0219 | <0.0245 | <0.148 | 1.57 | 0.055 |
| K2-03.14 | 179.5 | Core | 28.28 | 1076.93 | <0.0199 | <0.0266 | <0.032 | <0.156 | 0.827 | 0.593 |
| K2-03.21 | 243.9 | Rim | 85.86 | 1075.11 | <0.031 | <0.03 | <0.0229 | 0.197 | 0.643 | <0.050 |
| **K2-03.22** | 123.4 | Core | 173.26 | 1313.44 | <0.0245 | 0.034 | 0.0241 | 0.633 | 5.86 | <0.029 |
| **Mb1-04.10** | 185.5 | Core | 193.81 | 196.28 | 0.025 | <0.0214 | 0.0419 | 1.25 | 9.29 | 0.324 |
| **Mb1-04.13** | 155.2 | Core | 3.33 | 144.31 | <0.035 | <0.03 | 0.0311 | <0.071 | 0.156 | 0.274 |
| Mb1-04.15 | 163.4 | Core | 99.92 | 130.77 | <0.031 | <0.026 | <0.0202 | <0.141 | 0.7 | 0.357 |
| **Mb1-04.31** | 149.4 | Core | 231.52 | 130.46 | <0.0187 | <0.028 | <0.026 | 1.18 | 7.44 | 0.198 |
| Mb1-04.38 | 156.2 | Core | 60.45 | 55.61 | <0.027 | 0.2 | 0.121 | 2.03 | 3.54 | 2.08 |
| **X9-01.12** | 88.0 | Core | 13.94 | 54.18 | <0.0297 | <0.022 | <0.0099 | <0.060 | <0.100 | <0.047 |
| X9-01.19 | 97.4 | Core | 76.76 | 192.76 | <0.032 | <0.0213 | <0.0237 | 0.655 | 6.7 | 0.319 |
| **X9-01.24** | 113.7 | Core | 284.52 | 225.51 | 0.0269 | <0.030 | 0.034 | 0.667 | 7.06 | 0.189 |
| **X9-01.27** | 107.6 | Core | 37.98 | 292.44 | <0.0252 | 0.0308 | 0.0225 | <0.161 | 0.622 | 0.848 |
| **X9-01.29** | 131.3 | Core | 153.24 | 99.32 | <0.034 | 0.0258 | <0.039 | 0.251 | 4.48 | 0.556 |
| **X9-01.34** | 110.2 | Core | 226.74 | 45.18 | <0.0215 | 0.126 | 0.219 | 4.62 | 10.9 | 0.143 |
| **B1-05.16** | 160.8 | Core | 250.02 | 120.18 | 0.0239 | 0.131 | 0.108 | 3.34 | 8.1 | 0.19 |
| B1-05.35 | 80.1 | Core | 154.74 | 380.78 | 0.0235 | <0.042 | <0.0116 | <0.122 | 0.315 | 0.047 |
| **B1-05.37** | 88.0 | Core | 157.74 | 678.27 | <0.0258 | 0.0219 | 0.0248 | 0.311 | 3.22 | 0.073 |

(*continued on next page*)

**Table 3** (*continued*)

| Garnets | Gd | Tb | Dy | Ho | Er | Tm | Yb | Lu | ΣLREE | ΣHREE | Parent-rock Interpretation based on trace elements |
|---|---|---|---|---|---|---|---|---|---|---|---|
| **YCG-38.17** | 37.5 | 21.76 | 269.32 | 75.59 | 241.63 | 39.19 | 292.95 | 40.33 | 4.237 | 1018.27 | low-, medium-grade metapelites |
| **YCG-38.19** | 2.84 | 1.988 | 33.21 | 11.25 | 36.1 | 5.08 | 35.74 | 4.8 | 0.386 | 131.008 | low-, medium-grade metapelites |
| **YCG-38.36** | 0.925 | 0.68 | 20.91 | 11.8 | 60.16 | 11.7 | 92.48 | 11.07 | 0.122 | 209.725 | low-, medium-grade metapelites |
| YCG-17.14 | 1.25 | 0.367 | 3.01 | 0.761 | 2.1 | 0.301 | 2 | 0.157 | 0.732 | 9.946 | metabasic rocks |
| **YCG-17.16** | 3.57 | 2.013 | 30.18 | 11.66 | 48.07 | 7.56 | 56.38 | 7.32 | 0.815 | 166.753 | low-, medium-grade metapelites |
| **YCG-17.23** | 2.24 | 1.29 | 17.9 | 7.03 | 34.68 | 7.63 | 70.58 | 10.37 | 0.352 | 151.72 | low-, medium-grade metapelites |
| **YCG-17.30** | 3.18 | 3.18 | 60.16 | 23.49 | 81.94 | 12.94 | 92.46 | 12.9 | 0.192 | 290.25 | low-, medium-grade metapelites |
| **YCG-02.9** | 3.64 | 2.293 | 45.21 | 24.41 | 138.73 | 33.76 | 331.42 | 51.54 | 1.297 | 631.003 | low-, medium-grade metapelites |
| YCG-02.17 | 1.3 | 0.648 | 6.42 | 1.514 | 4.19 | 0.629 | 4.29 | 0.595 | 0.166 | 19.586 | metabasic rocks |
| YCG-02.25 | 11.54 | 3.48 | 21.02 | 4.08 | 10.55 | 1.477 | 10.45 | 1.485 | 3.296 | 64.082 | metabasic rocks |
| YCG-02.32 | 48.56 | 29.85 | 370.66 | 111.57 | 374.58 | 61.99 | 448.21 | 59.37 | 4.1012 | 1504.79 | intermediate-acidic igneous rocks |
| **YCG-02.34** | 1.06 | 0.344 | 2.46 | 0.491 | 1.318 | 0.153 | 0.888 | 0.137 | 1.182 | 6.851 | low-, medium-grade metapelites |
| **YCG-02.39** | 21.15 | 4.74 | 29.97 | 6.34 | 16.77 | 2.14 | 16.12 | 2.82 | 10.624 | 100.05 | low-, medium-grade metapelites |
| YCG-08.3 | 2.15 | 1.061 | 13.86 | 4.65 | 16.79 | 2.7 | 20.06 | 2.96 | 0.422 | 64.231 | metabasic rocks |
| YCG-08.5 | 3.35 | 0.731 | 6.36 | 1.849 | 5.57 | 0.891 | 5.81 | 0.8 | 6.041 | 25.361 | metabasic rocks |
| **YCG-08.24** | 4.98 | 1.996 | 19.9 | 5.17 | 13.91 | 1.777 | 12.79 | 1.39 | 1.2732 | 61.913 | low-, medium-grade metapelites |
| **YCG-08.30** | 3.55 | 1.067 | 10.07 | 2.27 | 5.25 | 0.673 | 4.36 | 0.53 | 0.301 | 27.77 | low-, medium-grade metapelites |
| YCG-08.32 | 2.31 | 0.833 | 8.85 | 2.81 | 8.78 | 1.258 | 7.03 | 0.731 | 1.068 | 32.602 | metabasic rocks |
| YCG-08.34 | 4.28 | 2.177 | 19.98 | 4.01 | 9.41 | 1.053 | 5.84 | 0.695 | 0.733 | 47.445 | metabasic rocks |
| S81–01.1 | 10.32 | 7.17 | 94.48 | 30.75 | 118.9 | 23.03 | 195.46 | 28.17 | 0.482 | 508.28 | intermediate-acidic igneous rocks |
| **S81-01.4** | 9.23 | 3.62 | 37.88 | 10 | 29.36 | 4.63 | 32.69 | 4.66 | 2.0562 | 132.07 | low-, medium-grade metapelites |
| S81–01.12 | 3.04 | 2.39 | 42.27 | 20.47 | 118.19 | 31.35 | 338.3 | 56.58 | 1.074 | 612.59 | intermediate-acidic igneous rocks |
| **S81-01.14** | 32.03 | 13.25 | 102.11 | 22.42 | 58.53 | 7.74 | 47.64 | 5.34 | 2.7907 | 289.06 | intermediate-acidic igneous rocks |
| S81–01.15 | 3.67 | 0.359 | 1.29 | 0.254 | 1.058 | 0.153 | 1.06 | 0.094 | 3.0189 | 7.938 | high-grade granulite-facies metapelites |
| **S81-01.21** | 16.4 | 2.53 | 11.9 | 1.91 | 4.62 | 0.552 | 3.68 | 0.34 | 7.574 | 41.932 | low-, medium-grade metapelites |
| S81–01.25 | 20.39 | 14.27 | 198.96 | 54.5 | 162.21 | 25.35 | 182.96 | 25.67 | 1.5542 | 684.31 | intermediate-acidic igneous rocks |
| **S81-01.26** | 111.57 | 31.79 | 157.49 | 14.37 | 19.63 | 1.94 | 9.38 | 0.691 | 39.222 | 346.861 | intermediate-acidic igneous rocks |
| S81–01.28 | 1.32 | 0.286 | 0.936 | 0.128 | 0.166 | <0.0260 | 0.123 | <0.028 | 0.7938 | 2.959 | high-grade granulite-facies metapelites |
| L87–09.21 | 17.74 | 6.13 | 47.26 | 10.69 | 28.81 | 3.65 | 24.71 | 3.25 | 4.0593 | 142.24 | high-grade granulite-facies metapelites |
| **K2-03.1** | 5.04 | 3.18 | 38.86 | 10.78 | 38.26 | 7.75 | 70.44 | 8.75 | 0.367 | 183.06 | low-, medium-grade metapelites |

(*continued on next page*)

**Table 3** (*continued*)

| Garnets | Gd | Tb | Dy | Ho | Er | Tm | Yb | Lu | ΣLREE | ΣHREE | Parent-rock Interpretation based on trace elements |
|---|---|---|---|---|---|---|---|---|---|---|---|
| K2-03.2 | 17.34 | 12.72 | 151.2 | 38.89 | 131.36 | 25.52 | 225.02 | 29.99 | 1.2645 | 632.04 | intermediate-acidic igneous rocks |
| K2-03.5 | 19.15 | 7.15 | 31.43 | 3.16 | 5.46 | 0.774 | 5.4 | 0.596 | 3.6832 | 73.12 | low-, medium-grade metapelites |
| **K2-03.9** | 29.56 | 15.32 | 146.18 | 32.76 | 98.92 | 17.01 | 137.97 | 17.95 | 4.1558 | 495.67 | intermediate-acidic igneous rocks |
| **K2-03.13** | 17.21 | 9.37 | 109.35 | 35.23 | 139.72 | 27.1 | 240.07 | 41.85 | 1.625 | 619.9 | intermediate-acidic igneous rocks |
| K2-03.14 | 11.63 | 9.47 | 137.68 | 42.83 | 122.97 | 16.37 | 101.09 | 12.7 | 1.42 | 454.74 | intermediate-acidic igneous rocks |
| K2-03.21 | 12.02 | 8.04 | 121.08 | 47.6 | 199.69 | 38.31 | 332.72 | 51.89 | 0.84 | 811.35 | intermediate-acidic igneous rocks |
| **K2-03.22** | 41.02 | 21.76 | 195.06 | 38.43 | 116.32 | 23.85 | 228.86 | 30.11 | 6.5511 | 695.41 | intermediate-acidic igneous rocks |
| **Mb1-04.10** | 23.13 | 4.73 | 33.25 | 7.52 | 23.25 | 3.53 | 27.32 | 3.87 | 10.9309 | 126.6 | high-grade granulite-facies metapelites |
| **Mb1-04.13** | 3.46 | 1.83 | 21.59 | 5.42 | 15.64 | 2.2 | 13.44 | 1.67 | 0.4611 | 65.25 | low-, medium-grade metapelites |
| Mb1-04.15 | 9.45 | 2.82 | 22.4 | 4.92 | 14.51 | 2.25 | 15.26 | 2.13 | 1.057 | 73.74 | low-, medium-grade metapelites |
| **Mb1-04.31** | 17.27 | 4.04 | 23.71 | 4.75 | 11.46 | 1.41 | 9.12 | 1.181 | 8.818 | 72.941 | high-grade granulite-facies metapelites |
| Mb1-04.38 | 7.54 | 1.478 | 10.1 | 2.19 | 5.88 | 0.812 | 6.17 | 0.755 | 7.971 | 34.925 | metabasic rocks |
| **X9-01.12** | <0.158 | 0.096 | 3.33 | 1.87 | 10.15 | 2.26 | 14.57 | 2 | 0 | 34.276 | low-, medium-grade metapelites |
| X9-01.19 | 16.95 | 3.87 | 29.75 | 7.37 | 23.42 | 3.76 | 29.34 | 4.66 | 7.674 | 119.12 | low-, medium-grade metapelites |
| **X9-01.24** | 24 | 5.67 | 38.46 | 8.43 | 23.49 | 3.6 | 25.57 | 3.71 | 7.9769 | 132.93 | high-grade granulite-facies metapelites |
| **X9-01.27** | 8.46 | 3.55 | 38.51 | 11.24 | 37.25 | 5.82 | 43.42 | 6.42 | 1.5233 | 154.67 | low-, medium-grade metapelites |
| **X9-01.29** | 14.16 | 2.67 | 18.53 | 3.8 | 11.01 | 1.66 | 12.02 | 1.78 | 5.3128 | 65.63 | high-grade granulite-facies metapelites |
| **X9-01.34** | 13.04 | 2.11 | 9.56 | 1.5 | 2.92 | 0.393 | 2.45 | 0.305 | 16.008 | 32.278 | high-grade granulite-facies metapelites |
| **B1-05.16** | 16.73 | 3.36 | 22.11 | 4.56 | 12.65 | 1.82 | 13.36 | 1.85 | 11.8929 | 76.44 | high-grade granulite-facies metapelites |
| B1-05.35 | 7.48 | 5.95 | 60.26 | 13.01 | 45.73 | 10.91 | 117.27 | 17.56 | 0.3855 | 278.17 | high-grade granulite-facies metapelites |
| **B1-05.37** | 22.35 | 11.06 | 99.26 | 20.82 | 62.25 | 11.22 | 95.06 | 13.17 | 3.6507 | 335.19 | intermediate-acidic igneous rocks |

The garnet grains marked as boldface indicate the same parent-rock interpretation as the interpretation based on the method by Tolosana-Delgado et al. (2018) (for details see Table 2).

[a] Measure the length of X axis (long axis) and Z axis (short axis) of the analyzed detrital garnet grains in the picture of garnet. Consider that the length of Y axis is equal to that of Z axis, and calculate the cube root the product of three length axes to obtain the equivalent spherical diameter (ESD) of this garnet grain (Huang et al., 2019).

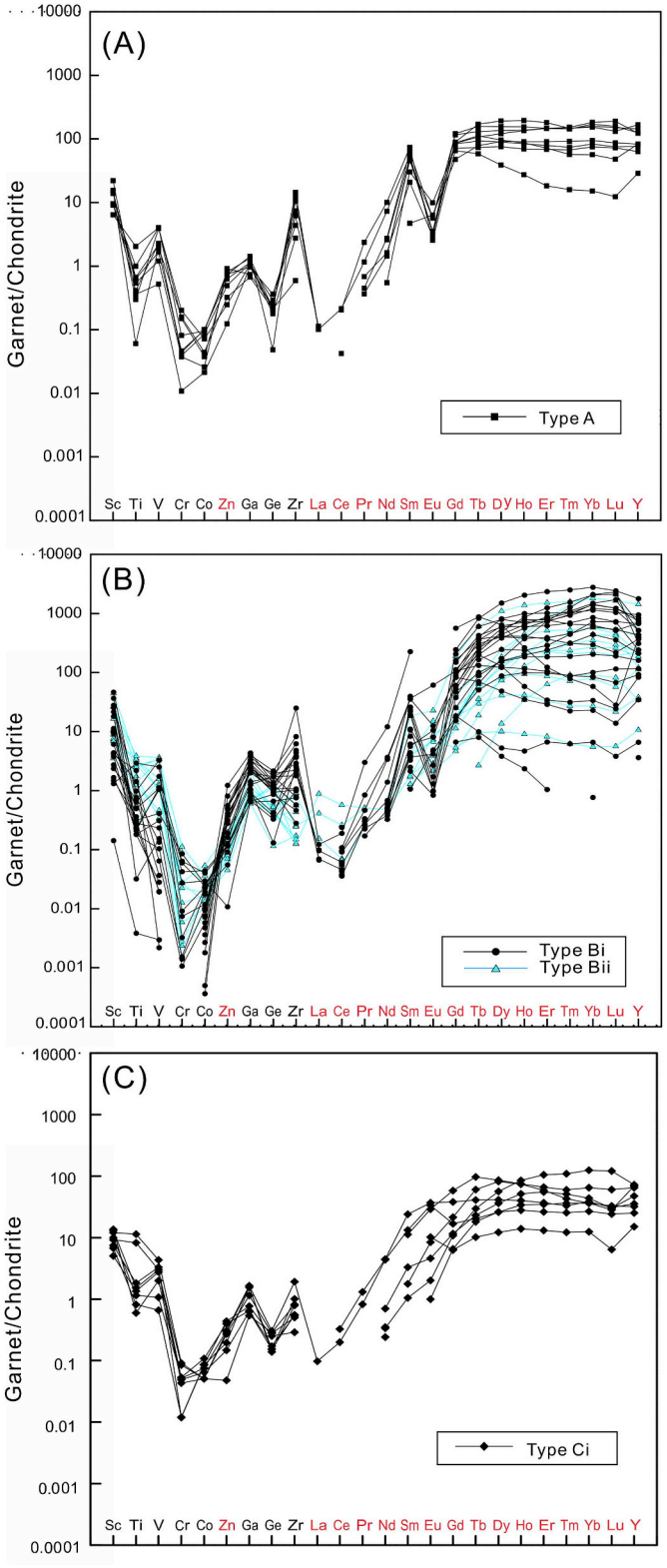


**Fig. 5.** Trace elements spider diagrams for the analyzed detrital garnets. (A): type A garnets; (B): type Bi and type Bii garnets; (C): type Ci garnets (according to the above major element results of Mange and Morton (2007)). Chondrite data are from McDonough and Sun (1995).

relatively homogeneous chemical composition (please see the BSE images in Fig. B4 in Appendix B). All these findings imply that the geochemical differences within a single garnet grain seem to be negligible and thus analysis on core or rim parts does not influence the provenance interpretations for most detrital garnets.

It is worth noting that some garnets from granulite-facies metapelites display MREE enrichment patterns (Fig. 6A). Hence, we favor that detrital garnets with $Gd_N/Yb_N > 1$ are most likely derived from granulite-facies metapelites rather than low-grade metapelites or intermediate-acidic igneous rocks (Fig. B5 in Appendix B). Besides, yttrium (Y) element generally shows higher content in granitic garnet. The range of Y content in granitic garnet is 315–3532 ppm, while the Y content range of garnets from metapelites is 0.4–836 ppm (Fig. 6C). Therefore, we propose that detrital garnets with Y content >800 ppm

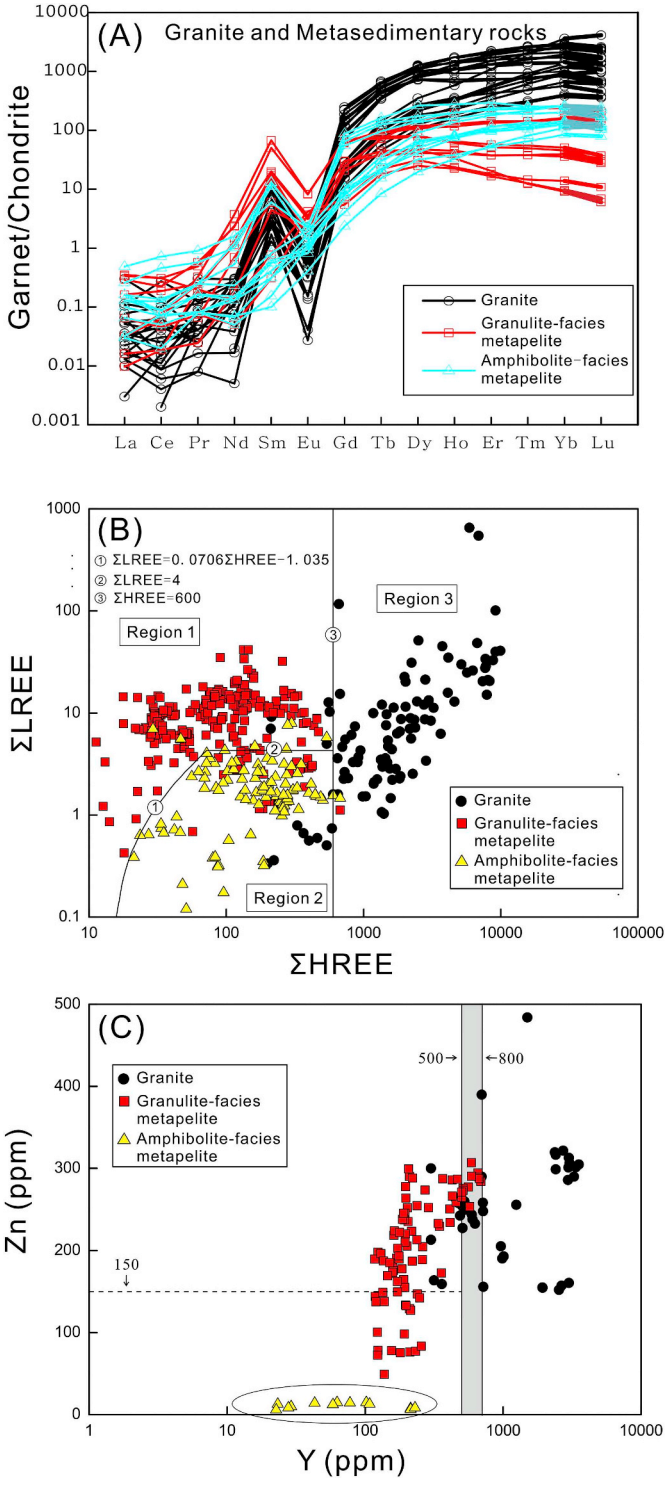


*(caption on next page)*

**Fig. 6.** The diagrams of garnet elements characteristic parameters from different felsic crystalline rocks. (A) REE features of garnets from granite and metapelite rocks. (B) ΣLREE and ΣHREE contents of garnets from granite and metapelite. Region 1: granulite-facies metapelites (taken up the total number of 94% collected granulite-facies metapelites garnets), region 2: amphibolite-facies metapelites (taken up the total number of 84% collected low-, medium-grade metapelites garnets), region 3: granite (taken up the total number of 86% collected granite garnets). (C) Zn and Y contents of garnets from granite and metapelite. Granite garnet data derived from Gao et al. (2012), Hönig et al. (2014), du Bray (1988), Jung and Hellebrand (2006), Villaros et al. (2009), Xu et al. (2013), Yang et al. (2013). Granulite-facies metapelite garnet data derived from Bea et al. (1997, 1999), Hermann and Rubatto (2003), Buick et al. (2010), Taylor and Stevens (2010), Orejana et al. (2011), Clarke et al. (2013), Jiao et al. (2013). Amphibolite-facies metapelite garnet data derived from Bea et al. (1997, 1999), Buick et al. (2010), Orozbaev et al. (2015), Gulbin (2016). These dashed and solid lines are our empirical values according to the collected data.

are likely derived from granites, detrital garnets with Y content of 500–800 ppm are probably derived from granites or metapelites, detrital garnets with Y content <500 ppm are likely derived from metapelites.

We hold the opinion that more detailed parent-rock discrimination for felsic crystalline rocks-derived garnet and the application of other trace elements in detrital garnet provenance analysis may deserve further consideration. A case study on Cenozoic granites and metapelites in the Himalayan orogenic belt suggests that garnets from granites have much higher Zn contents (>150 ppm) than garnets from metapelites (<100 ppm) (Gao et al., 2012). However, the collected data indicate that garnets from granulite-facies metapelites have similar Zn contents with granitic garnets (Jiao et al., 2013) and Zn contents of granulite-facies and amphibolite-facies garnets are different (Fig. 6C). Thus, the element Zn also shows possible utilizability on the garnet provenance discrimination.

### 5.2. Garnet trace elements in ultramafic rocks and skarn

Garnet is common in metabasic and ultramafic rocks (Zhang et al., 2006; Song et al., 2007a, 2007b). Magnesium-rich detrital garnets from ultramafic and metabasic rocks could well be distinguished on the basis of garnet major element composition (Mange and Morton, 2007; Tolosana-Delgado et al., 2018). However, determination of specific ultramafic parent rock remains poorly known. For example, garnets in peridotite and pyroxenite might have similar major element composition but have different trace element composition. Garnets from peridotites show sinusoidal REE distribution pattern and relatively higher in $Pr_N/Ho_N$ ratios (Fig. B6, Table A3) (Zhang et al., 2000; Burgess and Harte, 2004; Luo et al., 2004; Liati and Gebauer, 2009; Agashev et al., 2013; Pokhilenko et al., 2015). In addition, an overwhelmingly high Ca content is regarded as the dominant feature for garnet in skarn. Previous studies indicate that the garnets in different types of skarns show two main REE patterns (Fig. B7, Table A3). These can be concluded as a magma type: LREE enrichment, HREE depletion, positive Eu anomaly (indicates rich iron and oxidation environment) and a contact metasomatic type: LREE depletion, HREE enrichment, negative Eu anomaly (indicates rich aluminum and reducing environment) (Xiao and Liu, 2002; Gaspar et al., 2008; Zheng et al., 2012; Wang, 2016). These findings indicate that trace element geochemistry also displays a high potential in detailed provenance interpretation for ultramafic and skarn-sourced detrital garnets.

### 5.3. Revisiting detrital garnet provenance of the Cenozoic sandstones from the northern Qaidam basin

Combined with petrography, heavy mineral analysis and mineral chemical data, Jian et al., 2013a found significant spatial variations in the Cenozoic sandstone composition and thus proposed three depocenters (areas A, B and C, Fig. 1C) with different parent-rocks in the northern Qaidam basin. Sedimentary rocks in area A (Fig. 1C) were likely derived from multiple sources with a relatively long transport distance; and their parent-rocks are mainly metamorphic rocks of different grades and intermediate-acidic igneous rocks. The major parent-rocks of sedimentary rocks in area B are medium-low metamorphic rocks and high-grade metamorphic rocks; and the sediments source can be constrained within the North Qaidam and South Qilian metamorphic belts. Sedimentary rocks in area C (Fig. 1C) were mainly sourced from basic rocks, intermediate or acidic igneous rocks with subordinate metamorphic rocks (i.e., schists and gneisses).

The trace element characteristic parameters of the selected 51 detrital garnet grains from the northern Qaidam basin are shown in Fig. 8. Fe + Mn-rich, Mg-rich, Ca-poor (Type A in the diagram of Mange and Morton (2007)) garnets fell into the granulite-facies metapelites field in the ΣLREE-ΣHREE diagram (Fig. 8A). And they have less than 5% spessartine content, Zn content >150 ppm, Y content <500 ppm (Fig. 8B), supporting that these garnets were most likely derived from high-grade granulite-facies metapelites. As expected, most of the Fe + Mn-rich, Mg-poor, variable Ca (Type Bii in the diagram of Mange and Morton (2007)) garnets are plotted in the amphibolite-facies metapelite field, indicating the dominant source of amphibolite-facies metapelitic rocks or other low-, medium-grade metapelitic rocks. Some Fe + Mn-rich, Mg-poor, Ca-poor (Type Bi in the diagram of Mange and

**Table 4**
REE characteristic parameters of garnet in different granites and metapelitic rocks.

| Type | ΣLREE(ppm) | ΣHREE(ppm)(no Y) | Eu/Eu* | $Gd_N/Yb_N$ | $Sm_N/Gd_N$ |
|---|---|---|---|---|---|
| leucogranite | 0.34-3.28 | 200.8–1836.8 | 0.002-0.034 | 0.008-0.176 | 0.047-0.175 |
| A-type granite | 3.4–40.78 | 2029.5–9951.1 | 0.008-0.03 | 0.027-0.302 | 0.087-0.181 |
| peraluminous granitoid | 12.75–116.63 | 557–5917.5 | 0.002-0.487 | 0.071-0.397 | 0.121-0.365 |
| medium-grained biotite granite | 2.53–545.9 | 701.3–7913.7 | 0.001-0.004 | 0.019-0.176 | 0.117-0.673 |
| fine-grained two-mica granite | 2.85–101.34 | 1462.6–9172.6 | 0.001-0.002 | 0.017-0.189 | 0.123-0.682 |
| S-type granite | 1.3–7 | 211.2–771.7 | 0.133-0.251 | 0.044-0.245 | 0.151-0.346 |
| granulite-facies metapelite | 0.426-41.730 | 3.089–676.760 | 0.006-1.440 | 0.102-11.266 | 0.015-0.948 |
| amphibolite-facies metapelite | 0.120-7.933 | 21.226–1661.22 | 0.102-1.151 | 0.012-4.503 | 0.038-0.348 |

1) Leucogranite garnet data from Gao et al. (2012); 2) A-type garnet data derived from Hönig et al. (2014); 3) Peraluminous granitoid garnet data derived from du Bray (1988); 4) Medium-grained biotite granite and fine-grained two-mica granite garnet data derived from Yang et al. (2013); 5) S-type garnet data from Villaros et al. (2009). 6) Granulite-facies metapelite garnet data derived from Hermann and Rubatto (2003), Bea et al. (1997, 1999), Jiao et al. (2013), Orejana et al. (2011), Taylor and Stevens (2010), Clarke et al. (2013), Buick et al. (2010). 7) Amphibolite-facies metapelite garnet data derived from Bea et al. (1997, 1999), Buick et al. (2010), Orozbaev et al. (2015), Gulbin (2016). $Gd_N/Yb_N$ is used to indicate the degree of MREE enrichment.

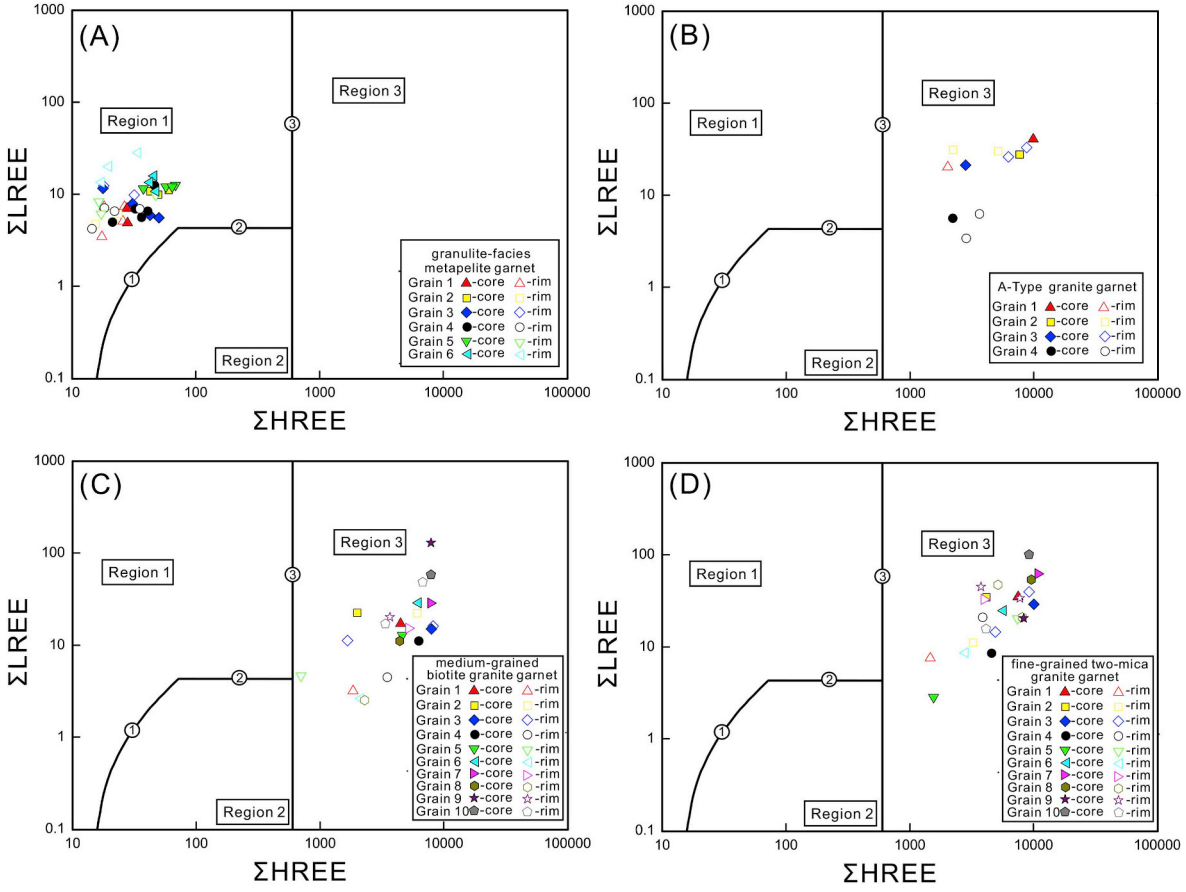


**Fig. 7.** ΣHREE-ΣLREE plots for core and rim parts of single garnet grains from different rocks. (A) garnet grains of granulite-facies metapelites (data from Zhang et al. (2015)). (B) garnet grains of A-Type granites (data from Hönig et al. (2014)). (C-D) garnet grains of a medium-grained biotite granite and a fine-grained two-mica granite (data from Yang et al. (2013)). This illustration highlights that the geochemical differences within a single garnet grain seem to be negligible and thus analysis on core or rim parts does not impact the provenance interpretations for most detrital garnets.

Morton (2007)) garnets, which were interpreted to be from intermediate to felsic igneous rocks, fell into the amphibolite-facies metapelite field (Fig. 8A). The results of Zn and Y contents (Fig. 8B) also support that these garnets are most likely derived from amphibolite-facies metapelites or other low-, medium-grade metapelites, rather than intermediate to felsic igneous rocks. Furthermore, the trace element cluster analysis results also reinforce the proposition that these garnets were most likely derived from different-grade metapelites (Table A5). Our new provenance interpretation is quite consistent with the interpretation results based on the discrimination method of Tolosana-Delgado et al. (2018) (The comparison results are shown in Table 3). Note that only a small amount of Type Bi garnets are plotted in the granite field. Therefore, the new provenance analysis results suggest that the detrital garnets in Cenozoic sedimentary rocks in the northern Qaidam were mainly derived from different-grade metapelitic rocks. Furthermore, Type Ci garnets (grains YCG-17.14, YCG-08.03, YCG-08.05, YCG-08.32, YCG-08.34, YCG-02.17, YCG-02.25, Mb1-04.38) are interpreted to be derived from metabasic rocks in the diagram of Mange and Morton (2007), whereas these detrital garnets are interpreted to be possibly from granulite-facies metapelites or amphibolite-facies metapelites (the possibilities are around 50%), based on the discrimination scheme of Tolosana-Delgado et al. (2018). The 8 Mg-rich, Ca-rich detrital garnets are also plotted in the discrimination diagram of ΣLREE-ΣHREE (Fig. 8A) and the results indicate that 5 grains therein have the same parent-rock interpretation to the evaluation depending on the method by Tolosana-Delgado et al. (2018). Hence, how trace element geochemistry comes into play in detailed provenance interpretation for Mg-rich, Ca-rich detrital garnets (i.e. probably of metabasic rock origin) remains an open question.

As the Qilian orogenic belt is a metamorphic belt and is mainly composed of schists and gneisses and other metamorphic rocks (Gehrels et al., 2003; Song et al., 2003a,b, 2005, 2006; Yang et al., 2006; Song et al., 2007a,b; Wang et al., 2009; Zhang et al., 2009), we suggest that the Lower Cenozoic sedimentary rocks in the Depositional area C (Fig. 1C), which is located in the northwestern corner of the Qaidam basin, close to the Altun Mountains and Qilian Mountains, likely had a major derivation of the Qilian orogenic belt. The trace element composition of the analyzed detrital garnets, discriminated by our new diagram, also show well match with the limited, published garnet trace element data of granulite-facies and amphibolite-facies metapelites and eclogites from the Qilian Mountains (Fig. 9). The new provenance interpretation is reinforced by paleocurrent data, which show dominant west- and southwest-directed paleoflow in the northern Qaidam basin (Zhuang et al., 2011; Jian et al., 2018; Lu et al., 2018). This means that the Altun Mountains, bounded by an active left-lateral strike-slip fault system separating the Qaidam basin from the Tarim basin (Fig. 1), did not uplift and were not in a high relief to feed detritus to the Qaidam basin during the early Cenozoic. Therefore, based on the new provenance interpretation in this study, we favor the proposition that the major tectonic deformation along the Altyn Tagh Fault, was dominated

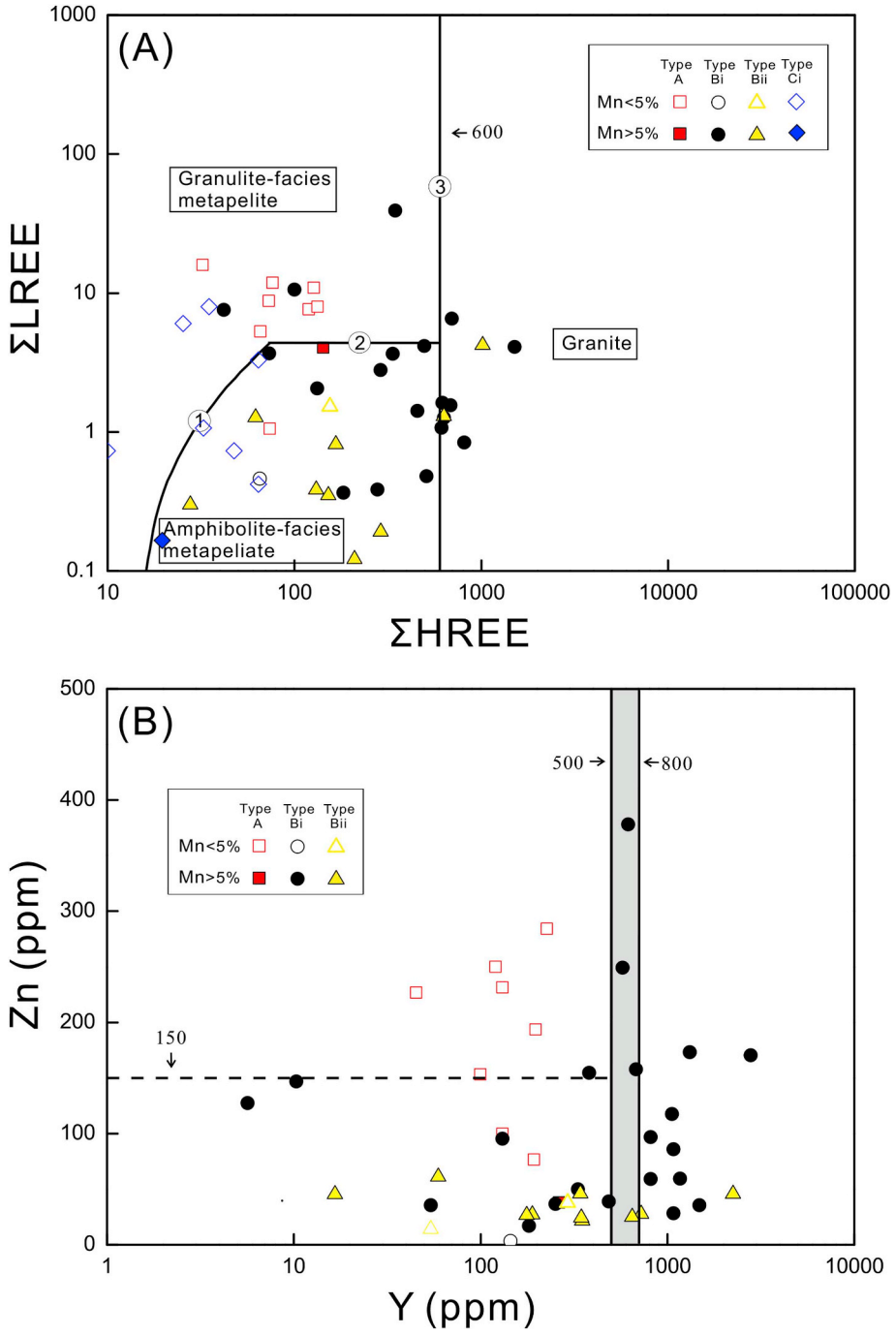


**Fig. 8.** Trace element discrimination diagrams for the analyzed detrital garnets of the Cenozoic sandstone samples from the northern Qaidam basin. (A) ΣLREE-ΣHREE plots of the analyzed garnets. (B) Zn-Y plots of the analyzed garnets.

by large-amplitude lateral offset and extrusion, rather than crustal thickening and uplift in the early Cenozoic (Yue and Liou, 1999; Yue et al., 2003; Lu et al., 2016; Jian et al., 2018).

## 6. Conclusions

We collected published trace element data of garnets from granites and different-grade metapelites and compared these data with the detrital garnet composition obtained from the Cenozoic sediments of the Qaidam basin, northern Tibet to explore the potential of detrital garnet trace element geochemistry in sedimentary provenance analysis. The following conclusions can be drawn from the present study:

(1) The REE and Y elements could be employed to distinguish garnets derived from intermediate-acidic igneous rocks and different-grade metapelites. Generally, garnet from granites have high Y and HREE contents, while garnet from metapelites has low Y and HREE contents. Garnet derived from granulite-facies metapelites usually has higher ΣLREE and Zn contents, while garnet derived from amphibolite-facies metapelites has lower ΣLREE and Zn contents. These findings are an important step towards a better understanding of trace element geochemistry in detrital garnet provenance analysis.
(2) Fe + Mn-rich garnets in the Cenozoic sedimentary rocks from the northern Qaidam basin were alternatively interpreted to be sourced from intermediate-acidic igneous rocks or metapelites. Here,

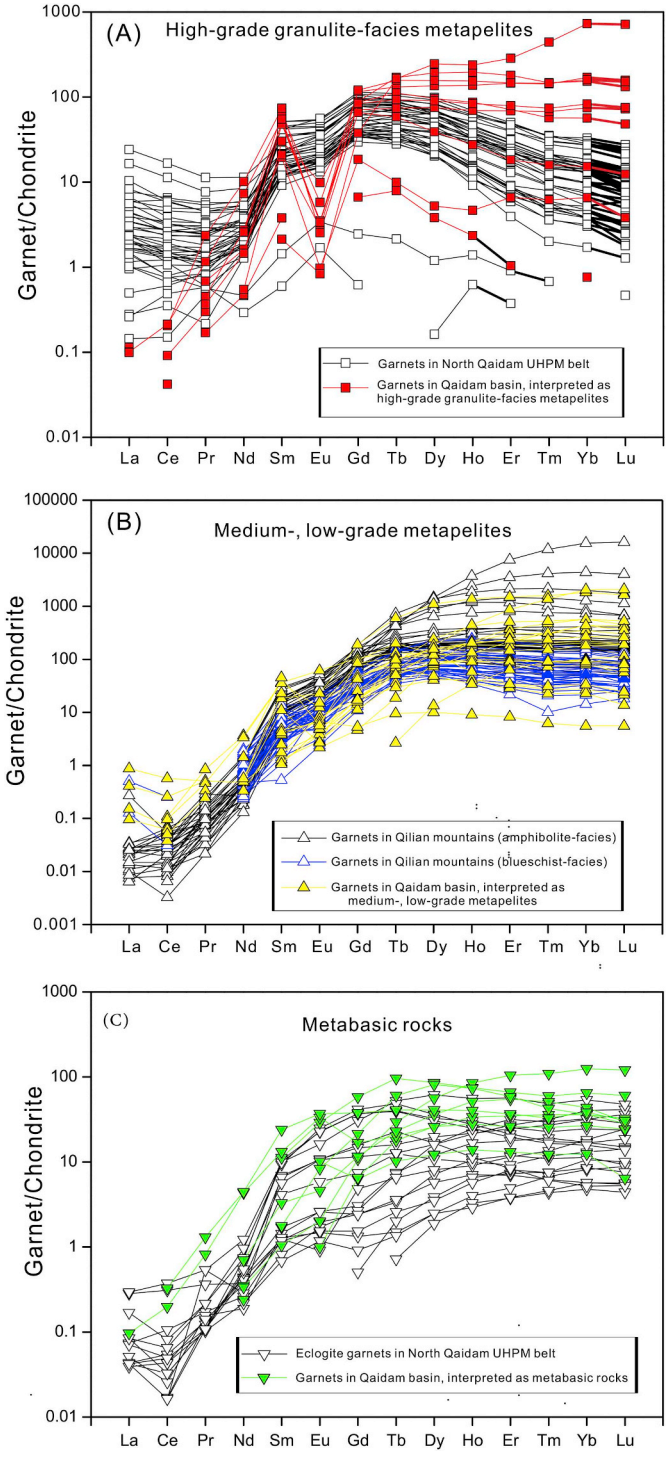


**Fig. 9.** REE patterns of garnets from potential parent-rocks in the Qilian Mountains. The REE data of the analyzed detrital garnets (classified based on the new parent-rock interpretation) from the Cenozoic Qaidam basin are also involved. (A) Granulite-facies metapelites from the North Qaidam UHPM belt (Zhang et al., 2015); (B) amphibolite-facies and blueschist-facies metapelites garnet data derived from the Qilian mountains (Mattinson et al., 2009; Xiao et al., 2013; Cheng et al., 2016) and (C) eclogite from the North Qaidam UHPM belt (Zhang et al., 2013, 2015).

however, most of these garnets were likely derived from metapelites, based on the new trace element geochemical data.

(3) The northern Qaidam basin was dominantly fed by the Qilian metamorphic belt rather by than the Altun Mountains during the early Cenozoic. This means that the Altun Mountains had not experienced extensive uplift and had not formed high relief to the Qaidam basin in the early Cenozoic.

## CRediT authorship contribution statement

**Dongming Hong:** Investigation, Methodology, Visualization, Writing - original draft, Writing - review & editing. **Xing Jian:** Conceptualization, Funding acquisition, Supervision, Validation, Writing - original draft, Writing - review & editing. **Ling Fu:** Writing - original draft, Writing - review & editing. **Wei Zhang:** Resources, Writing - original draft, Project administration, Writing - review & editing.

## Declaration of competing interest

We declare that we don't have any conflict of interest.

## Acknowledgments

This work is supported by National Natural Science Foundation of China (No. 41806052, 41902126), Natural Science Foundation of Fujian Province (No. 2017J05067) and Xiamen University Fundamental Research Funds for the Central Universities (Nos. 20720190097, 20720190103). We would like to thank Prof. Ping Guan, Dr. Fan Feng, Ruijian Liu of Peking University for helping the field work. We also appreciate Dr. Fang Ma for her help in sample preparation and laboratory analysis. We are grateful to four anonymous reviewers for their detailed and constructive peer-review comments, which greatly improved the quality of this paper.

## Appendix A. Supplementary data

Supplementary data to this article can be found online at https://doi.org/10.1016/j.marpetgeo.2020.104316.

## References

Agashev, A.M., Ionov, D.A., Pokhilenko, N.P., Golovin, A.V., Cherepanova, Y., Sharygina, I.S., 2013. Metasomatism in lithospheric mantle roots: constraints from whole-rock and mineral chemical composition of deformed peridotite xenoliths from kimberlite pipe Udachnaya. Lithos 160–161 (1), 201–215. https://doi.org/10.1016/j.lithos.2012.11.014.

Aubrecht, R., Méres, Š., Sýkora, M., Mikus, T., 2009. Provenance of the detrital garnets and spinels from the albian sediments of the Czorsztyn unit (Pieniny Klippen belt, western Carpathians, Slovakia). Geol. Carpathica 60 (6), 463–483. https://doi.org/10.2478/v10096-009-0034-z.

Basei, M.A.S., Frimmel, H.E., Nutman, A.P., Preciozzi, F., Jacob, J., 2005. A connection between the Neoproterozoic Dom Feliciano (Brazil/Uruguay) and Gariep (Namibia/South Africa) orogenic belts - evidence from a reconnaissance provenance study. Precambrian Res. 139 (3), 195–221. https://doi.org/10.1016/j.precamres.2005.06.005.

Basu, A., 2003. A perspective on quantitative provenance analysis. Quant. Provenance Stud. Italy 61, 11–22.

Bea, E., 1996. Residence of REE, Y, Th and U in granites and crustal protoliths; implications for the chemistry of crustal melts. J. Petrol. 37, 521–552. https://doi.org/10.1093/petrology/37.3.521.

Bea, F., Montero, P., 1999. Behavior of accessory phases and redistribution of Zr, REE, Y, Th, and U during metamorphism and partial melting of metapelites in the lower crust: an example from the Kinzigite Formation of Ivrea-Verbano, NW Italy. Geochem. Cosmochim. Acta 63 (7–8), 1133–1153. https://doi.org/10.1016/S0016-7037(98)00292-0.

Bea, F., Montero, P., Garuti, G., Zaccarini, F., 1997. Pressure-dependence of rare earth element distribution in amphibolite- and granulite-grade garnets. ALA-ICP-MS study. Geostand. Geoanal. Res. 21 (2), 253–270. https://doi.org/10.1111/j.1751-908X.1997.tb00674.x.

Bhatia, M.R., 1983. Plate tectonics and geochemical composition of sandstone. J. Geol. 91 (6), 611–627. https://doi.org/10.1086/628921.

Blatt, H., 1967. Provenance determinations and recycling of sediments. J. Sediment. Res. 37 (4), 1031–1044. https://doi.org/10.1306/74D71825-2B21-11D7-8648000102C1865D.

Bonova, K., Bona, J., Kovacik, M., Mikus, T., 2018. Heavy minerals and exotic pebbles from the Eocene flysch deposits of the Magura Nappe (Outer Western Carpathians, eastern Slovakia): their composition and implications on the provenance. Turk. J.

Earth Sci. 27 (1), 64–88. https://doi.org/10.3906/yer-1707-9.
Buick, I.S., Clark, C., Rubatto, D., Hermann, J., Pandit, M., Hand, M., 2010. Constraints on the Proterozoic evolution of the Aravalli–Delhi Orogenic belt (NW India) from monazite geochronology and mineral trace element geochemistry. Lithos 120 (3), 511–528. https://doi.org/10.1016/j.lithos.2010.09.011.
Burgess, S.R., Harte, B., 2004. Tracing lithosphere evolution through the analysis of heterogeneous G9–G10 garnets in peridotite xenoliths, II: REE chemistry. J. Petrol. 45 (3), 609–633. https://doi.org/10.1093/petrology/egg095.
Cheng, H., Lu, T., Cao, D., 2016. Coupled Lu–Hf and Sm–Nd geochronology constrains blueschist-facies metamorphism and closure timing of the Qilian Ocean in the North Qilian orogen. Gondwana Res. 34, 99–108. https://doi.org/10.1016/j.gr.2016.03.008.
Chetel, L.M., Simo, J.A., Singer, B.S., 2005. 40Ar/39Ar geochronology and provenance of detrital K-feldspars, Ordovician, Upper Mississippi Valley. Sediment. Geol. 182 (1), 163–181. https://doi.org/10.1016/j.sedgeo.2005.07.010.
Chew, D.M., Sylvester, P.J., Tubrett, M.N., 2011. U–Pb and Th–Pb dating of apatite by LA-ICPMS. Chem. Geol. 280 (1–2), 200–216. https://doi.org/10.1016/j.chemgeo.2010.11.010.
Clarke, G.L., Daczko, N.R., Miescher, D., 2013. Identifying relic igneous garnet and clinopyroxene in eclogite and granulite, Breaksea Orthogneiss, New Zealand. J. Petrol. 54 (9), 1921–1938. https://doi.org/10.1093/petrology/egt036.
Clift, P.D., Shimizu, N., Layne, G.D., Blusztajn, J., 2001. Tracing patterns of erosion and drainage in the Paleogene Himalaya through ion probe Pb isotope analysis of detrital K-feldspars in the Indus Molasse, India. Earth Planet Sci. Lett. 188 (3), 475–491. https://doi.org/10.1016/S0012-821X(01)00346-6.
Condie, K.C., Belousova, E., Griffin, W.L., Sircombe, K.N., 2009. Granitoid events in space and time: constraints from igneous and detrital zircon age spectra. Gondwana Res. 15 (3–4), 228–242. https://doi.org/10.1016/j.gr.2008.06.001.
Čopjaková, R., Sulovský, P., Paterson, B.A., 2005. Major and trace elements in pyropealmandine garnets as sediment provenance indicators of the Lower Carboniferous Culm sediments, Drahany Uplands, Bohemian Massif. Lithos 2005 82 (1), 51–70. https://doi.org/10.1016/j.lithos.2004.12.006.
Coutand, I., Carrapa, B., Deeken, A., Schmitt, A., Sobel, E.R., Strecker, M.R., 2010. Propagation of orographic barriers along an active range front: insights from sandstone petrography and detrital apatite fission-track thermochronology in the intramontane Angastaco basin, NW Argentina. Basin Res. 18 (1), 1–26. https://doi.org/10.1111/j.1365-2117.2006.00283.x.
Dickinson, W.R., 1970. Interpreting detrital modes of graywacke and arkose. J. Sediment. Petrol. 40, 695–707. https://doi.org/10.1306/74D72018-2B21-11D7-8648000102C1865D.
Dickinson, W.R., 1985. Interpreting provenance relations from detrital modes of sandstones. In: Zuffa, G.G. (Ed.), Provenance of Arenites. Reidel Publ., Dordrecht, pp. 333–361.
Dickinson, W.R., 1988. Provenance and sediment dispersal in relation to paleotectonics and paleogeography of sedimentary basins. In: Kleinspehn, K.L., Paola, C. (Eds.), New Perspectives in Basin Analysis. Frontiers in Sedimentary Geology, pp. 3–25.
Dill, H.G., 1995. Heavy mineral response to the progradation of an alluvial fan: implications concerning unroofing of source area, chemical weathering and palaeo-relief (Upper Cretaceous Parkstein fan complex, SE Germany). Sediment. Geol. 95 (1–2), 39–56. https://doi.org/10.1016/0037-0738(94)00096-D.
Dorais, M.J., Tubrett, M., 2012. Detecting peritectic garnet in the peraluminous Cardigan Pluton, New Hampshire. J. Petrol. 53, 299–324. https://doi.org/10.1093/petrology/egs014.
du Bray, E.A.D., 1988. Garnet compositions and their use as indicators of peraluminous granitoid petrogenesis-southeastern Arabian Shield. Contrib. Mineral. Petrol. 100 (2), 205–212. https://doi.org/10.1007/BF00373586.
Faryad, S.W., Jedlicka, R., Hauzenberger, C., Racek, M., 2018. High-pressure crystallization vs. recrystallization origin of garnet pyroxenite-eclogite within subduction related lithologies. Mineral. Petrol. 112 (5), 603–616. https://doi.org/10.1007/s00710-018-0557-z.
Fedo, C.M., Sircombe, K.N., Rainbird, R.H., 2003. Detrital zircon analysis of the sedimentary record. Rev. Mineral. Geochem. 53 (1), 277–303. https://doi.org/10.2113/0530277.
Gao, L.E., Zeng, L.S., Shi, W.G., Chen, Z.Y., Hu, M.Y., Sun, D.Y., 2012. Two types of garnets in the Cenozoic granites from the Himalayan Orogenic belt: geochemical characteristics and implications for crustal anatexis. Acta Petrol. Sin. 28 (9), 2963–2980 (in Chinese) 1000-0569/2012/028(09)-2963-80.
Garzanti, E., Resentini, A., Ando, S., Vezzoli, G., Pereira, A.J.S.C., Vermeesch, P., 2015. Physical controls on sand composition and relative durability of detrital minerals during ultra-long distance littoral and aeolian transport (Namibia and southern Angola). Sedimentology 62 (4), 971–996. https://doi.org/10.1111/sed.12169.
Gaspar, M., Knaack, C., Meinert, L.D., Moretti, R., 2008. REE in skarn systems: a LA-ICP-MS study of garnets from the Crown Jewel gold deposit. Geochem. Cosmochim. Acta 72 (1), 185–205. https://doi.org/10.1016/j.gca.2007.09.033.
Gehrels, G.E., Yin, X., Wang, X.F., 2003. Magmatic history of the northeastern Tibetan Plateau. J. Geophys. Res. 108 (B9), 2423. https://doi.org/10.1029/2002jb001876.
Gillespie, J., Glorie, S., Khudoley, A., Collins, A.S., 2018. Detrital apatite U-Pb and trace element analysis as a provenance tool: insights from the Yenisey Ridge (Siberia). Lithos 314, 140–155. https://doi.org/10.1016/j.lithos.2018.05.026.
Gulbin, Y.L., 2016. Zonal REE + Y profiles in garnet and their genetic implications: a case study of metapelites from the northern Ladoga region. Geol. Ore Deposits 58 (7), 559–567. https://doi.org/10.1134/S1075701516070035.
Harrison, T.M., Copeland, P., Kidd, W.S.F., Yin, A., 1992. Raising Tibet. Science 255, 1663–1670. https://doi.org/10.1126/science.255.5052.1663.
Henry, D.J., Guidotti, C.V., 1985. Tourmaline as a petrogenetic indicator mineral: an example from the staurolite-grade metapelites of NW Maine. Am. Mineral. 70, 1–15.
Hermann, J., Rubatto, D., 2003. Relating zircon and monazite domains to garnet growth zones: age and duration of granulite facies metamorphism in the Val Malenco lower crust. J. Metamorph. Geol. 21 (9), 833–852. https://doi.org/10.1046/j.1525-1314.2003.00484.x.
Hietpas, J., Samsom, S., Speir, J., Moecher, D., 2014. Assessing detrital garnet chemical composition as A quantitative provenance tool: a multivariate statistical approach. J. Sediment. Res. 83 (12), 1181–1197. https://doi.org/10.2110/jsr.2013.83.
Hönig, S., Čopjaková, R., Škoda, R., Novák, M., Dolejs, D., Leichmann, J., Galiová, M.V., 2014. Garnet as a major carrier of the Y and REE in the granitic rocks: an example from the layered anorogenic granite in the Brno Batholith, Czech Republic. Am. Mineral. 99 (10), 1922–1941. https://doi.org/10.2138/am-2014-4728.
Huang, X., Jian, X., Zhang, W., Hong, D.M., Guan, P., Du, J.X., 2019. Detrital garnet geochemistry-based provenance analysis and interpretation: the effect of grain size. Acta Sedimentol. Sin. 37 (3), 511–518. https://doi.org/10.14027/j.issn.1000-0550.2018.161. (in Chinese).
Huber, B., Bahlburg, H., Pfänder, J.A., 2018. Single grain heavy mineral provenance of garnet and amphibole in the Surveyor fan and precursor sediments on the Gulf of Alaska abyssal plain—implications for climate-tectonic interactions in the St. Elias orogen. Sediment. Geol. 372, 173–192. https://doi.org/10.1016/j.sedgeo.2018.05.007.
Hurst, A., Morton, A.C., 1988. An application of heavy-mineral analysis to lithostratigraphy and reservoir modelling in the Oseberg Field, northern North Sea. Mar. Petrol. Geol. 5 (2), 157–169. https://doi.org/10.1016/0264-8172(88)90020-7.
Ingersoll, R.V., Bullard, T.F., Ford, R.L., Grimm, J.P., Pickle, J.D., Sares, S.W., 1984. The effect of grain size on detrital modes: a test of the Gazzi–Dickinson point-counting method. J. Sediment. Petrol. 54, 103–116. https://doi.org/10.1306/212F8783-2B24-11D7-8648000102C1865D.
Jian, X., 2013. Controls on Mesozoic and Cenozoic Sedimentary Evolution of the Northern Qaidam Basin: Tectonic and Climatic Implications. Peking University PhD dissertation.
Jian, X., Guan, P., Fu, S.T., Zhang, D.W., Zhang, W., Zhang, Y.S., 2014. Miocene sedimentary environment and climate change in the northwestern Qaidam basin, northeastern Tibetan plateau: facies, biomarker and stable isotopic evidences. Palaeogeogr. Palaeoclimatol. Palaeoecol. 414, 320–331. https://doi.org/10.1016/j.palaeo.2014.09.011.
Jian, X., Guan, P., Zhang, W., Fan, F., 2013b. Geochemistry of Mesozoic and Cenozoic sediments in the northern Qaidam basin, northeastern Tibetan Plateau: implications for provenance and weathering. Chem. Geol. 360 (361), 74–88. https://doi.org/10.1016/j.chemgeo.2013.10.011.
Jian, X., Guan, P., Zhang, W., Liang, H.H., Feng, F., Fu, L., 2018. Late Cretaceous to early Eocene deformation in the northern Tibetan Plateau: detrital apatite fission track evidence from northern Qaidam basin. Gondwana Res. 60, 94–104. https://doi.org/10.1016/j.gr.2018.04.007.
Jian, X., Guan, P., Zhang, D.W., Zhang, W., Feng, F., Liu, R.J., Lin, S.D., 2013a. Provenance of Tertiary sandstone in the northern Qaidam basin, northeastern Tibetan Plateau: integration of framework petrography, heavy mineral analysis and mineral chemistry. Sediment. Geol. 290, 109–125. https://doi.org/10.1016/j.sedgeo.2013.03.010.
Jian, X., Weislogel, A., Pullen, A., 2019a. Triassic sedimentary filling and closure of the eastern Paleo-Tethys ocean: new insights from detrital zircon geochronology of Songpan-Ganzi, Yidun and west Qinling flysch in eastern Tibet. Tectonics. https://doi.org/10.1029/2018TC005300.
Jian, X., Zhang, W., Liang, H.H., Guan, P., Fu, L., 2019b. Mineralogy, petrography and geochemistry of an early Eocene weathering profile on basement granodiorite of Qaidam basin, northern Tibet: tectonic and paleoclimatic implications. Catena 172, 54–64. https://doi.org/10.1016/j.catena.2018.07.029.
Jiao, S., Guo, J., Harley, S.L., Peng, P., 2013. Geochronology and trace element geochemistry of zircon, monazite and garnet from the garnetite and/or associated other high-grade rocks: implications for Palaeoproterozoic tectonothermal evolution of the Khondalite Belt, North China Craton. Precambrian Res. 237, 78–100. https://doi.org/10.1016/j.precamres.2013.09.008.
Johnsson, M.J., 1993. The system controlling the composition of clastic sediments. In: In: Johnsson, M.J., Basu, A. (Eds.), Processes Controlling the Composition of Clastic Sediments Geological Society of America, Special Paper, vol. 284. pp. 1–19.
Jung, S., Hellebrand, E., 2006. Trace element fractionation during high-grade metamorphism and crustal melting—constraints from ion microprobe data of metapelitic, migmatitic and igneous garnets and implications for Sm–Nd garnet chronology. Lithos 87 (3–4), 193–213. https://doi.org/10.1016/j.lithos.2005.06.013.
Krippner, A., Meinhold, G., Morton, A.C., von Eynatten, H., 2014. Evaluation of garnet discrimination diagrams using geochemical data of garnets derived from various host rocks. Sediment. Geol. 306 (6), 36–52. https://doi.org/10.1016/j.sedgeo.2014.03.004.
Lenaz, D., Kamenetsky, V.S., Princivalle, F., 2003. Cr-spinel supply in the Brkini, Istrian and Krk island flysch basins (Slovenia, Italy and Croatia). Geol. Mag. 140 (3), 335–342. https://doi.org/10.1016/S0375-6742(99)00029-1.
Lenaz, D., Mazzoli, C., Spišiak, J., Princivalle, F., Maritan, L., 2009. Detrital Cr-spinel in the Šambron–Kamenica zone (Slovakia): evidence for an ocean-spreading zone in the northern Vardar suture? Int. J. Earth Sci. 98 (2), 345–355. https://doi.org/10.1007/s00531-007-0243-6.
Lenaz, D., Mazzoli, C., Velicogna, M., Princivalle, F., 2018. Trace and Rare Earth Elements chemistry of detrital garnets in the SE Alps and Outer Dinarides flysch basins: an important tool to better define the source areas of sandstones. Mar. Petrol. Geol. 98, 653–661. https://doi.org/10.1016/j.marpetgeo.2018.09.025.
Li, Z., Song, W., Peng, S., Wang, D., Zhang, Z., 2004. Mesozoic–Cenozoic tectonic relationships between the Kuqa subbasin and Tian Shan, northwest China: constraints from depositional records. Sediment. Geol. 172, 223–249. https://doi.org/10.1016/j.

sedgeo.2004.09.002.
Liati, A., Gebauer, D., 2009. Crustal origin of zircon in a garnet peridotite: a study of U-Pb SHRIMP dating, mineral inclusions and REE geochemistry (Erzgebirge, Bohemian Massif). Eur. J. Mineral 21 (4), 737–750. https://doi.org/10.1127/0935-1221/2009/0021-1939.
Lu, H., Fu, B., Shi, P., Ma, Y., Li, H., 2016. Constraints on the uplift mechanism of northern Tibet. Earth Planet Sci. Lett. 453, 108–118. https://doi.org/10.1016/j.epsl.2016.08.010.
Lu, H., Ye, J., Guo, L., Pan, J., Xiong, S., Li, H., 2018. Towards a clarification of the provenance of Cenozoic sediments in the northern Qaidam Basin. Lithosphere, 2018 11 (2), 252–272. https://doi.org/10.1130/L1037.1.
Luo, Y., Gao, S., Yuan, H.L., Liu, X.M., Gunther, D., Jin, Z.M., Sun, M., 2004. Mineral Ce anomaly in Dabie - Sulu eclogite and garnet pyroxene: tracer of deep subduction of sediments in oxidized environment. Sci. China Earth Sci. 34 (1), 14–23. https://doi.org/10.3321/j.issn:1006-9267.2004.01.002. (In Chinese).
Mange, M.A., Morton, A.C., 2007. Geochemistry of heavy minerals. In: In: Mange, M.A., Wright, D.T. (Eds.), Heavy Minerals in Use: Developments in Sedimentology, vol. 58. pp. 345–391.
Mattinson, C.G., Wooden, J.L., Liou, J.G., Bird, D.K., Wu, C.L., 2006. Age and duration of eclogite-facies metamorphism, North Qaidam HP/UHP terrane, western China. Am. J. Sci. 306, 683–711. https://doi.org/10.1016/j.gca.2006.06.809.
Mattinson, C.G., Menold, C.A., Zhang, J.X., Bird, D.K., 2007. High and ultrahigh pressure metamorphism in The north Qaidam and south Altyn terranes, western China. Int. Geol. Rev. 49, 969–995. https://doi.org/10.2747/0020-6814.49.11.969.
Mattinson, C.G., Wooden, J.L., Zhang, J.X., Bird, D.K., 2009. Paragneiss zircon geochronology and trace element geochemistry, North Qaidam HP/UHP terrane, western China. J. Asian Earth Sci. 35, 298–309. https://doi.org/10.1016/j.jseaes.2008.12.007.
McDonough, W.F., Sun, S.S., 1995. The composition of the Earth. Chem. Geol. 120 (3–4), 223–253. https://doi.org/10.1016/0009-2541(94)00140-4.
McLennan, S.M., Hemming, S., Mcdaniel, D.K., Hanson, G.N., 1993. Geochemical approaches to sedimentation, provenance, and tectonics. Spec. Pap. Geol. Soc. Am. 284, 21–40. https://doi.org/10.1130/SPE284-p21.
Meinhold, G., 2010. Rutile and its applications in earth sciences. Earth Sci. Rev. 102 (1), 1–28. https://doi.org/10.1016/j.earscirev.2010.06.001.
Meinhold, G., Anders, B., Kostopoulos, D., Reischmann, T., 2008. Rutile chemistry and thermometry as provenance indicator: an example from Chios Island, Greece. Sediment. Geol. 203 (1–2), 98–111. https://doi.org/10.1016/j.sedgeo.2007.11.004.
Meinhold, G., Reischmann, T., Kostopoulos, D., Frei, D., Larionov, A.N., 2010. Mineral chemical and geochronological constraints on the age and provenance of the eastern Circum-Rhodope Belt low-grade metasedimentary rocks, NE Greece. Sediment. Geol. 229, 207–223. https://doi.org/10.1016/j.sedgeo.2010.06.007.
Menold, C.A., Manning, C.E., Yin, A., Tropper, P., Chen, X.H., Wang, X.F., 2009. Metamorphic evolution, mineral chemistry and thermobarometry of orthogneiss hosting ultra high pressure eclogites in the North Qaidam metamorphic belt, Western China. J. Asian Earth Sci. 35, 273–284. https://doi.org/10.1016/j.jseaes.2008.12.008.
Morton, A.C., 1985. A new approach to provenance studies: electron microprobe analysis of detrital garnets from Middle Jurassic sandstones of the northern North Sea. Sedimentology 32, 553–566. https://doi.org/10.1111/j.1365-3091.1985.tb00470.x.
Morton, A.C., Hallsworth, C., 1994. Identifying provenance-specific features of detrital heavy mineral assemblages in sandstones. Sediment. Geol. 90 (3–4), 241–256. https://doi.org/10.1016/0037-0738(94)90041-8.
Morton, A.C., Hallsworth, C.R., 1999. Processes controlling the composition of heavy mineral assemblages in sandstones. Sediment. Geol. 124 (1–4), 3–29. https://doi.org/10.1016/S0037-0738(98)00118-3.
Morton, A.C., Hallsworth, C.R., 2007. Stability of detrital heavy minerals during burial diagenesis. In: Mange, M.A., Wright, D.T. (Eds.), Heavy Minerals in Use. vol. 58. Developments in sedimentology, pp. 215–245.
Morton, A.C., 1993. Heavy Minerals in Colour by M. a. Mange and H. F. W. Maurer. Chapman and Hall, London, vol. 1991. pp. 147. https://doi.org/10.1002/gj.3350280212. price £55.00. isbn 0412439107. Geological Journal, 28(2), 211-212.
Morton, A.C., Claouelong, J.C., Hallsworth, C.R., 2001. Zircon age and heavy mineral constraints on provenance of North Sea Carboniferous sandstones. Mar. Petrol. Geol. 18 (3), 319–337. https://doi.org/10.1016/S0264-8172(00)00065-9.
Morton, A.C., Hallsworth, C., Chalton, B., 2004a. Garnet compositions in Scottish and Norwegian basement terrains: a framework for interpretation of North Sea sandstone provenance. Mar. Petrol. Geol. 21 (3), 393–410. https://doi.org/10.1016/j.marpetgeo.2004.01.001.
Morton, A.C., Hallsworth, C.R., Chalton, B., 2004b. Garnet compositions in Scottish and Norwegian basement terrains: a framework for interpretation of North Sea sandstone provenance. Mar. Petrol. Geol. 21, 393–410. https://doi.org/10.1016/j.marpetgeo.2004.01.001.
Morton, A.C., Whitham, A.G., Fanning, C.M., 2005. Provenance of Late Cretaceous to Paleocene submarine fan sandstones in the Norwegian Sea: integration of heavy mineral, mineral chemical and zircon age data. Sediment. Geol. 182, 3–28. https://doi.org/10.1016/j.sedgeo.2005.08.007.
Morton, A.C., Meinhold, G., Howard, J.P., Phillips, R.J., Strogen, D., Abutarruma, Y., Elgadry, M., Thusu, B., Whitham, A.G., 2011. A heavy mineral study of sandstones from the eastern margin of the Murzuq Basin, Libya: constraints on provenance and stratigraphic correlation. J. Afr. Earth Sci. 61, 308–330. https://doi.org/10.1016/j.jafrearsci.2011.08.005.
Müller, A., Kaersley, A., Spratt, J., Seltmann, R., 2012. Petrogenetic impli- cations of magmatic garnet in granitic pegmatites from southern Norway. Can. Mineral. 50, 1095–1115. https://doi.org/10.3749/canmin.50.4.1095.
Noble, T.L., Piotrowski, A.M., Robinson, L.F., Mcmanus, J.F., Hillenbrand, C.D., Bory, M., 2012. Greater supply of Patagonian-sourced detritus and transport by the ACC to the Atlantic sector of the Southern Ocean during the last glacial period. Earth Planet Sci. Lett. 317–318 (2), 374–385. https://doi.org/10.1016/j.epsl.2011.10.007.
Orejana, D., Villaseca, C., Armstrong, R.A., Teresa, E., Jeffries, 2011. Geochronology and trace element chemistry of zircon and garnet from granulite xenoliths: constraints on the tectonothermal evolution of the lower crust under central Spain. Lithos 124 (1–2), 103–116. https://doi.org/10.1016/j.lithos.2010.10.011.
Orozbaev, R., Hirajima, T., Bakirov, A., Takasu, A., Maki, K., Yoshida, K., Sakiev, K., Bakirov, A., Hirata, T., Tagiri, M., Togonbaeva, A., 2015. Trace element characteristics of clinozoisite pseudomorphs after lawsonite in talc-garnet-chloritoid schists from the Makbal UHP Complex, northern Kyrgyz Tian-Shan. Lithos 226, 98–115. https://doi.org/10.1016/j.lithos.2014.10.008.
Osae, S., Asiedu, D.K., Banoeng-Yakubo, B., Koeberl, C., Dampare, S.B., 2006. Provenance and tectonic setting of Late Proterozoic Buem sandstones of southeastern Ghana: evidence from geochemistry and detrital modes. J. Afr. Earth Sci. 44 (1), 85–96. https://doi.org/10.1016/j.jafrearsci.2005.11.009.
Pettijohn, F.J., 1963. Chemical Composition of Sandstones — Excluding Carbonate and Volcanic Sands. U.S. Geol. Survey Professional Paper 400–S, pp. 19.
Pokhilenko, N.P., Agashev, A.M., Litasov, K.D., Pokhilenko, L.N., 2015. Carbonatite metasomatism of peridotite lithospheric mantle: implications for diamond formation and carbonatite-kimberlite magmatism. Russ. Geol. Geophys. 56 (1–2), 280–295. https://doi.org/10.1016/j.rgg.2015.01.020.
Romans, B., Castelltort, S., Covault, J.A., Filedani, A., Walsh, J.P., 2016. Environmental signal propagation in sedimentary systems across timescales. Earth Sci. Rev. 153, 7–29. https://doi.org/10.1016/j.earscirev.2015.07.012.
Ross, G.M., Parrish, R.R., 1991. Detrital zircon geochronology of metasedimentary rocks in the southern Omineca Belt, Canadian Cordillera. Can. J. Earth Sci. 28 (8), 1254–1270. https://doi.org/10.1139/e91-112.
Sevigny, J.H., 1993. Monazite controlled Sm/Nd fractionation in leucogranites: an Ion microprobe study of garnet phenocrysts. Geochem. Cosmochim. Acta 57, 4095–4102. https://doi.org/10.1016/0016-7037(93)90355-Z.
Smeds, S.A., 1994. Zoning and fractionation trends of a peraluminous NYF granitic pegmatite field at Falun, south-central Sweden. GFF (J. Geol. Soc. Sweden) 116 (3), 175–184. https://doi.org/10.1080/11035899409546181.
Song, S.G., Yang, J.S., Xu, Z.Q., Liou, J.G., Wu, C.L., Shi, R.D., 2003a. Metamorphic evolution of coesite-bearing UHP terrane in the North Qaidam, northern Tibet, NW China. J. Metamorph. Geol. 21, 631–644. https://doi.org/10.1046/j.1525-1314.2003.00469.x.
Song, S.G., Yang, J.S., Liou, J.G., Wu, C.L., Shi, R.D., Xu, Z.Q., 2003b. Petrology, geochemistry and isotopic ages of eclogites in the Dulan UHPM terrane, The north Qaidam, NWChina. Lithos 70, 195–211. https://doi.org/10.1016/S0024-4937(03)00099-9.
Song, S.G., Zhang, L.F., Niu, Y.L., Su, L., Jian, P., Liu, D.Y., 2005. Geochronology of diamond-bearing zircons from garnet peridotite in the North Qaidam UHPM belt Northern Tibetan Plateau: a record of complex histories from oceanic lithosphere subduction to continental collision. Earth Planet Sci. Lett. 234, 99–118. https://doi.org/10.1016/j.epsl.2005.02.036.
Song, S.G., Zhang, L.F., Niu, Y.L., Su, L., Song, B., Liu, D.Y., 2006. Evolution from oceanic subduction to continental collision: a case study of the Northern Tibetan Plateau inferred from geochemical and geochronological data. J. Petrol. 47, 435–455. https://doi.org/10.1093/petrology/egi080.
Song, S., Su, L., Niu, Y., Zhang, L., Zhang, G., 2007a. Petrological and geochemical constraints on the origin of garnet peridotite in the North Qaidam ultrahigh-pressure metamorphic belt, northwestern China. Lithos 96, 243–265. https://doi.org/10.1016/j.lithos.2006.09.017.
Song, S.G., Zhang, L.F., Niu, Y., Wei, C.J., Liou, J.G., Shu, G.M., 2007b. Eclogite and carpholite-bearing metasedimentary rocks in the North Qilian suture zone, NW China: implications for Early Palaeozoic cold oceanic subduction and water transport into mantle. J. Metamorph. Geol. 25, 547–563. https://doi.org/10.1111/j.1525-1314.2007.00713.x.
Sun, Z., Yang, Z., Pei, J., Ge, X., Wang, X., Yang, T., Li, W., Yuan, S., 2005. Magnetostratigraphy of Paleogene sediments from northern Qaidam Basin, China: implications for tectonic uplift and block rotation in northern Tibetan plateau. Earth Planet Sci. Lett. 237, 635–646. https://doi.org/10.1016/j.epsl.2005.07.007.
Takeuchi, M., Kawai, M., Matsuzawa, N., 2008. Detrital garnet and chromian spinel chemistry of Permian clastics in the Renge area, central Japan: implications for the paleogeography of the East Asian continental margin. Sediment. Geol. 212 (1–4), 25–39. https://doi.org/10.1016/j.sedgeo.2008.09.002.
Tapponnier, P., Xu, Z., Roger, F., Meyer, B., Arnaud, N., Wittlinger, G., Yang, J., 2001. Oblique stepwise rise and growth of the Tibet Plateau. Science 294, 1671–1677. https://doi.org/10.1126/science.105978.
Taylor, J., Stevens, G., 2010. Selective entrainment of peritectic garnet into S-type granitic magmas: evidence from Archaean mid-crustal anatectites. Lithos 120 (3–4), 277–292. https://doi.org/10.1016/j.lithos.2010.08.015.
Teraoka, Y., Suzuki, M., Hayashi, T., Kawakami, K., 1997. Detrital garnets from paleozoic and mesozoic sandstones in the onogawa area, east Kyushu, southwest Japan. Bull. Faculty School Educ. 19, 87–101.
Teraoka, Y., Suzuki, M., Kawakami, K., 1998. Provenance of Cretaceous and paleogene sediments in the median zone of southwest Japan. Bull. Geol. Surv. Jpn. 49, 395–411.
Tolosana-Delgado, R., von Eynatten, H., Krippner, A., Meinhold, G., 2018. A multivariate discrimination scheme of detrital garnet chemistry for use in sedimentary provenance analysis. Sediment. Geol. 375, 14–26. https://doi.org/10.1016/j.sedgeo.2017.11.003.
Triebold, S., von Eynatten, H., Luvizotto, G.L., Zack, T., 2007. Deducing source rock lithology from detrital rutile geochemistry: an example from the Erzgebirge, Germany. Chem. Geol. 244 (3–4), 421–436. https://doi.org/10.1016/j.chemgeo.2007.06.033.

Triebold, S., von Eynatten, H., Zack, T., 2012. A recipe for the use of rutile in sedimentary provenance analysis. Sediment. Geol. 282, 268–275. https://doi.org/10.1016/j.sedgeo.2012.09.008.

Vermunt, J.K., Magidson, J., 2002. Latent class cluster analysis. Appl. Latent Class Anal. 11, 89–106. https://doi.org/10.1007/978-94-007-0753-5_102221.

Villaros, A., Stevens, G., Buick, I.S., 2009. Tracking S-type granite from source to emplacement: clues from garnet in the Cape granite suite. Lithos 112 (3), 217–235. https://doi.org/10.1016/j.lithos.2009.02.011.

von Eynatten, H., Dunkl, I., 2012. Assessing the sediment factory: the role of single grain analysis. Earth Sci. Rev. 115, 97–120. https://doi.org/10.1016/j.earscirev.2012.08.001.

Wang, J.B., 2016. Characteristics and Origin of the Baocun Skarn Gold Deposit, Tongling, Anhui Province. China University of Geosciences, Beijing (In Chinese). CNKI:CDMD:2.1016.068230.

Wang, X., Qiu, Z., Li, Q., Wang, B., Qiu, Z., Downs, W.R., Xie, G., Xie, J., Deng, T., Takeuchi, G.T., Tseng, Z.J., Chang, M., Liu, J., Wang, Y., Biasatti, D., Sun, Z., Fang, X., Meng, Q., 2007. Vertebrate paleontology, biostratigraphy, geochronology, and paleoenvironment of Qaidam Basin in northern Tibetan Plateau. Palaeogeogr. Palaeoclimatol. Palaeoecol. 254, 363–385. https://doi.org/10.1016/j.palaeo.2007.06.007.

Wang, Q., Pan, Y., Chen, N., Li, X., Chen, H., 2009. Proterozoic polymetamorphism in the Quanji Block, northwestern China: evidence from microtextures, garnet compositions and monazite CHIME ages. J. Asian Earth Sci. 34, 686–698. https://doi.org/10.1016/j.jseaes.2008.10.008.

Weltje, G.J., von Eynatten, H., 2004. Quantitative provenance analysis of sediments: review and outlook. Sediment. Geol. 171 (1), 1–11. https://doi.org/10.1016/j.sedgeo.2004.05.007.

Whitworth, M.P., Feely, M., 1994. The compositional range of magmatic Mn-garnets in Galway Granite, Connemara, Ireland. Mineral. Mag. 58, 163–168. https://doi.org/10.1180/minmag.1994.058.390.16.

Xiao, C.D., Liu, X.W., 2002. REE geochemistry and origin of skarn garnets from eastern Inner Mongolia. Chin. Geol. 29 (3), 311–316. https://doi.org/10.3969/j.issn.1000-3657.2002.03.014. (In Chinese).

Xiao, Y., Niu, Y., Song, S., Davidson, J., Liu, X., 2013. Elemental responses to subduction-zone metamorphism: constraints from the North Qilian Mountain, NW China. Lithos 160, 55–67. https://doi.org/10.1016/j.lithos.2012.11.012.

Xu, L.J., Xiao, Y.L., Wu, F., Li, S.G., Simon, K., Wörner, G., 2013. Anatomy of garnets in a Jurassic granite from the south-eastern margin of the North China Craton: magma sources and tectonic implications. J. Asian Earth Sci. 78 (12), 198–221. https://doi.org/10.1016/j.jseaes.2012.11.026.

Yang, J.S., Wu, C.L., Zhang, J.X., Shi, R.D., Meng, F.C., Wooden, J., Yang, H.Y., 2006. Protolith of eclogites in the north Qaidam and Altun UHP terrane NW China: earlier oceanic crust? J. Asian Earth Sci. 28, 185–204. https://doi.org/10.1016/j.jseaes.2005.09.020.

Yang, J.H., Peng, J.T., Hu, R.Z., Bi, X.W., Zhao, J.H., Fu, Y.Z., Shen, N.P., 2013. Garnet geochemistry of tungsten-mineralized Xihuashan granites in South China. Lithos 177 (1), 79–90. https://doi.org/10.1016/j.lithos.2013.06.008.

Ye, D., Zhong, X., Yao, Y., Yang, F., Zhang, S., Jiang, Z., Wang, Y., 1993. Tertiary Strata in Chinese Petroliferous Provinces (Volume I) — the General. Petroleum Industry Press, Beijing, China, pp. 156–159 (in Chinese).

Yin, A., Rumelhart, P.E., Butler, R.E., Cowgill, E., Harrison, T.M., Foster, D.A., Ingersoll, R.V., Zhang, Q., Zhou, X.Q., Wang, X.F., Hanson, A., Raza, A., 2002. Tectonic history of the Altyn Tagh fault system in northern Tibet inferred from Cenozoic sedimentation. Geol. Soc. Am. Bull. 114, 1257–1295. https://doi.org/10.1130/0016-7606(2002)114<1257:THOTAT>2.0.CO;2.

Yue, Y., Liou, J.G., 1999. Two-stage evolution model for the Altyn Tagh fault, China. Geology 27, 227–230. https://doi.org/10.1130/0091-7613(1999)027<0227:TSEMFT>2.3.CO;2.

Yue, Y., Ritts, B.D., Graham, S.A., Wooden, J.L., Gehrels, G.E., Zhang, Z., 2003. Slowing extrusion tectonics: lowered estimate of post-Early Miocene slip rate for the Altyn Tagh fault. Earth Planet Sci. Lett. 217, 111–122. https://doi.org/10.1016/S0012-821X(03)00544-2.

Zhang, X.H., Gou, G.C., 1993. Tian Peizhao et al. The division of ancient plate and ground structure in Qilian Mountain and North Mt. area. NW. Geol. 14, 2 (In Chinese).

Zhang, H.F., Menzies, M.A., Lu, F.X., Zhou, X.H., 2000. The main and trace elements of garnet and garnet from Paleozoic mantle rock traps in north China. Sci. China Earth Sci. 30 (2), 128–134. https://doi.org/10.3321/j.issn:1006-9267.2000.02.003. (In Chinese).

Zhang, Z.M., Liou, J.G., Zhao, X.D., Shi, C., 2006. Petrogenesis of Maobei rutile eclogites from the southern Sulu ultrahigh-pressure metamorphic belt, eastern China. J. Metamorph. Geol. 24 (8), 15. https://doi.org/10.1111/j.1525-1314.2006.00665.x.

Zhang, G., Song, S., Zhang, L., Niu, Y., 2008. The subducted oceanic crust within continental-type UHP metamorphic belt in the North Qaidam, NW China: evidence from petrology, geochemistry and geochronology. Lithos 104, 99–118. https://doi.org/10.1016/j.lithos.2007.12.001.

Zhang, G., Zhang, L., Song, S., Niu, Y., 2009. UHP metamorphic evolution and SHRIMP geochronology of a coesite-bearing meta-ophiolitic gabbro in the North Qaidam, NW China. J. Asian Earth Sci. 35, 310–322. https://doi.org/10.1016/j.jseaes.2008.11.013.

Zhang, C., Zhang, L., Bader, T., Song, S., Lou, Y., 2013. Geochemistry and trace element behaviors of eclogite during its exhumation in the Xitieshan terrane, North Qaidam UHP belt, NW China. J. Asian Earth Sci. 63, 81–97. https://doi.org/10.1016/j.jseaes.2012.09.021.

Zhang, G., Niu, Y., Song, S., Zhang, L., Tian, Z., Christy, A.G., Han, L., 2015. Trace element behavior and P–T–t evolution during partial melting of exhumed eclogite in the North Qaidam UHPM belt (NW China): implications for adakite genesis. Lithos 226, 65–80. https://doi.org/10.1016/j.lithos.2014.12.009.

Zhang, W., Jian, X., Fu, L., Feng, F., Guan, P., 2018. Reservoir characterization and hydrocarbon accumulation in late Cenozoic lacustrine mixed carbonate-siliciclastic fine-grained deposits of the northwestern Qaidam basin, NW China. Mar. Petrol. Geol. 98, 675–686. https://doi.org/10.1016/j.marpetgeo.2018.09.008.

Zheng, Z., Du, Y.S., Cao, Y., Gao, Z.W., Yang, S., Dong, Q., 2012. The composition characteristics and origin of garnets in the Dongguashan skarn copper deposit, Anhui Province. Acta Petrol. Mineral. 31 (2), 235–242. https://doi.org/10.3969/j.issn.1000-6524.2012.02.011. (In Chinese).

Zhuang, G., Hourigan, J.K., Ritts, B.D., Kent-Corson, M.L., 2011. Cenozoic multiple-phase tectonic evolution of the northern Tibetan Plateau: constraints from sedimentary records from Qaidam basin, Hexi Corridor, and Subei basin, northwest China. Am. J. Sci. 311 (2), 116–152. https://doi.org/10.2475/02.2011.02.